

1 Importance of grain boundary processes for plasticity in the quartz-dominated crust: 2 Implications for flow laws

3 Subhajit Ghosh^{a,b*}, Holger Stünitz^{a,c}, Hugues Raimbourg^a, Jacques Précigout^a, Ida Di Carlo^a, Renée
4 Heilbronner^d, Laurette Piani^e

5 ^a
6 *Institut des Sciences de la Terre d'Orléans (ISTO), UMR7327, Université d'Orléans, CNRS, BRGM, ,
7 45071, Orléans, France*

8 ^b
9 *Department of Geology and Geophysics, Woods Hole Oceanographic Institution, Woods Hole, MA,
10 USA
11 ^cDepartment of Geology, University of Tromsø, Dramsveien 201, 9037, Tromsø, Norway*

12 ^d*Department of Environmental Sciences, Universität Basel, CH-4056 Basel, Switzerland*

13 ^e*Centre de Recherche Pétrographique et Géochimique (CRPG), UMR 7358, Université de
14 Lorraine, CNRS, Vandoeuvre-les-Nancy, France*

15 * Corresponding author: cugeol.subhajit@gmail.com (S. Ghosh)

16 Abstract

17 When H₂O is present along grain boundaries, the deformation processes responsible for plasticity
18 in silicate mineral aggregates can deviate from what may be conventionally expected.
19 Although a necessary component of understanding crustal deformation processes, there is
20 no theoretical framework that incorporates grain boundary processes into polycrystalline
21 quartz rheology. To address this issue, we carried out high-pressure and high-temperature
22 deformation experiments on fine-grained quartz aggregates. Our study illustrates that grain
23 boundary migration (GBM) through dissolution-precipitation (in the presence of an aqueous fluid)
24 and grain boundary sliding (GBS) may act as accommodation mechanisms to prevent hardening
25 from dislocation glide. GBM and GBS can relax incompatibilities resulting from an inadequate
26 number of independent slip systems, plastic anisotropy between neighbouring grains, and non-
27 planar grain boundaries together with grain boundary junctions. As demonstrated earlier in the
28 mechanism counteracting hardening, but also is a potential mechanism that allow H₂O to enter in the
29 quartz crystal (hydrolization) at the experimental time-scale. The above serial processes occur over a
30 range of more than two orders of magnitude in grain size (~3 to 200 μm) and explain a grain-size-
31 insensitive stress exponent ($n = 2$) and low activation energy ($Q = 110$ kJ/mol). In the absence of a
32 switch to grain size sensitive deformation mechanisms induced by grain size reduction, our results
33 imply that only a modest weakening (~5 times the strength of the protolith) is needed (or possible) to
34 localize shear zones in the Earth's crust.

35 **keywords:** Quartz rheology, Flow law, Grain Boundary Migration, Grain Boundary
36 Sliding, Hydrolytic weakening, core-shell-structure

37 1. Introduction

38 How parts of the crust become weaker compared to the surrounding rocks and develop into
39 plate boundaries is one of the fundamental questions when trying to explain plate tectonics on Earth.
40 In nature, weakening of silicate minerals involves two essential components: (a) the presence of H₂O,
41 and (b) reduced grain size (e.g., Griggs 1974; Bercovici and Ricard, 2016; Finch et al., 2016; Hirth

and Tullis, 1992; Kronenberg et al., 2020). Quartz is one of the best studied rock-forming minerals of the Earth's crust, and understanding quartz rheology and microstructures are instrumental to characterize the mechanical properties of crustal rocks (Hirth et al., 2001). Consequently, an overwhelming number of experimental studies have focused on establishing creep laws for coarse- and fine-grained natural and synthetic quartz aggregates in different hydrous conditions over the last four decades (e.g., Jaoul et al., 1984; Kronenberg and Tullis, 1984; Luan and Paterson, 1992; Gleason and Tullis, 1995; Rutter and Brodie, 2004a, 2004b; Fukuda et al., 2018; Richter et al., 2018). Recently, using the new generation hydraulically-driven Griggs-type apparatus, it has become possible to perform constant-load experiments with larger sample size at a regulated constant confining pressure (Précigout et al., 2018). New experiments have yielded flow-law parameters for wet (0.1 wt.% H₂O-added) coarse-grained (~200 μm) quartzite from the Tana quarry, Norway based on the following equation:

$$\dot{\epsilon} = A \left(\frac{\sigma^n}{d^p} \right) f_{H_2O}^r \exp\left(-\frac{Q}{RT}\right), \quad (1)$$

where $\dot{\epsilon}$ is the strain rate, σ is the differential stress, f_{H_2O} is the water fugacity term with an exponent $r = 1$, d is the grain size, n is the stress exponent, p is the grain size exponent, Q is the activation energy, and A is the pre-exponential term. The new flow law is as follows (Ghosh et al., 2022):

$$\dot{\epsilon} = 1.56 \times 10^{-9} /_{\text{MPa}/\text{sec}} \cdot \sigma^2 \cdot f_{H_2O} \cdot \exp\left(-\frac{110 \text{ kJ/mol}}{RT}\right).$$

Although a n -value lower than 3 has been obtained for other coarse-grained quartz materials (Jaoul et al., 1984; Koch et al., 1989; Luan and Paterson, 1992), it deviates from the accepted climb-controlled dislocation creep models with $n \approx 3-5$ (Hirth et al., 2001; Karato, 2008; Luan and Paterson, 1992; Paterson and Luan, 1990; Rutter and Brodie, 2004b). The n -values lower than 3 have been found for fine-grained quartz (Kronenberg and Tullis, 1984; Fukuda et al., 2018; Richter et al., 2018) and the contribution from diffusion creep ($n = 1$) (Herring, 1950; Nabarro, 1948; Coble, 1963) was interpreted to produce lower n -values (Fukuda et al., 2018; Richter et al., 2018). However, grain-size-exponent of $p = 2$ or 3 as in grain size sensitive deformation mechanisms has not been identified (Jaoul et al., 1984; Kronenberg and Tullis, 1984; Fukuda et al., 2018; Ghosh et al., 2022). On the other hand, the low grain size exponent of $p \approx 0.5$ (Fukuda et al. 2018) is difficult to interpret. It has been concluded that grain boundary processes including dissolution-precipitation and grain boundary sliding (GBS) can lower the n -value (Ghosh et al., 2022; Nègre et al., 2021; Pongrac et al., 2022, Richter et al., 2018; Tokle et al., 2019).

Earlier studies have shown that extremely dry quartz single crystals or polycrystalline quartz aggregates are too strong to deform plastically under laboratory conditions (Blacic and Christie, 1984; Griggs, 1974; Kronenberg and Tullis, 1984) and a certain amount of H₂O is required ('hydrolytic weakening') to induce plasticity (Griggs and Blacic, 1965). Water weakening of quartz is generally associated with molecular forms of H₂O and/or with dissociated forms of H₂O (Stünitz et al., 2017). It has been proposed that hydrolization of Si-O bounds is responsible for the water weakening by easing the dislocation glide process (Griggs and Blacic 1965; Griggs 1967; Griggs, 1974). Additionally, the weakening effect can be originated from dislocation generation and multiplication associated with microcracking, crack healing, and fluid inclusion decrepitation (Stünitz et al., 2017). These explanations are suitable in the case of a single crystal quartz. However, in a polycrystalline material, according to the von Mises criterion at least five independent sets of slip systems are needed to achieve homogeneous deformation dominantly by glide mechanism (Karato, 2008). Much fewer slip systems are actually activated in quartz (Pongrac et al., 2022; Tokle et al., 2019). Furthermore, grains

oriented in a favourable position for easy slip with respect to the local stress state will deform easily in comparison to the poorly oriented neighbouring grains (Qi et al., 2017). As a result, plastic incompatibilities between neighbouring grains can arise. To overcome these incompatibilities, additional processes (Hutchinson, 1977) such as grain boundary sliding (GBS) are needed, as shown in other geological materials like halite, ice, anorthite, and olivine (Bourcier et al., 2013, Dimanov et al., 2007, Goldsby and Kohlstedt, 2001; Hansen et al., 2011). GBS has also been speculated to operate in quartz (Ghosh et al., 2022; Tokle et al., 2019), even though non-planar grain boundaries together with grain boundary junctions impede GBS in normal circumstances (Ashby, 1972; Raj and Ashby, 1971). Therefore, for GBS to be an effective accommodation mechanism for crystal-plastic deformation by dislocation glide, there is a need for the activation of processes that counteract obstacles at grain boundaries.

The spectrum of quartz grain sizes found in natural rocks varies from coarse (millimeters) to very fine (a few micrometers). Therefore, the effect of the grain size on the mechanical properties (e.g., viscosity) of quartz aggregates is also an important factor to consider. For example, it is presumed that grain size reduction (GSR) in mylonitic shear zones can lead to significant weakening through the transition from grain-size-insensitive (GSI) to grain-size-sensitive (GSS) creep mechanisms (Schmid 1982; Rutter and Brodie, 1988) with n -value of 1. However, such a switch in dominant deformation mechanism has strictly been observed at a grain size of $\sim 1 \mu\text{m}$ in dry quartz experiments (Rutter and Brodie 2004b, Fukuda et al., 2018) giving rise to the possibility that the deformation mechanism in fine-grained quartz bearing rocks ($> 1 \mu\text{m}$) may not be comparable to other geological materials like olivine, anorthite, ice, and diopside at a similar grain size range (Dimanov et al., 2007; Goldsby and Kohlstedt, 2001; Hier-Majumder et al., 2005; Hirth and Kohlstedt, 2004).

When H_2O is present along grain boundaries, additional boundary processes (e.g. dissolution-precipitation) can be activated in natural rocks and may lead to a deviation from pure solid-state models of rate-limiting deformation processes in quartz (Karato, 2008; Paterson, 2012). A detailed microstructural and chemical investigation has been carried out to document the grain boundary processes in experimentally deformed quartz aggregates to bridge this gap in our knowledge. The naturally occurring fine-grained novaculite employed in this study (Fig. 1) has a 2D grain size of $3.80 \mu\text{m}$ (3D mode = $5.70 \mu\text{m}$). A similar range of sizes has been observed for dynamically recrystallized grains in an originally coarse-grained ($\sim 200 \mu\text{m}$) Tana quartzite deformed in previous studies (Nègre et al., 2021; Pongrac et al., 2022). Thus, novaculite may be considered as an example of a completely recrystallized material generated from a former coarse grained natural quartzite. Consequently, using novaculite in experiments, it is possible to quantify the influence of grain size reduction by recrystallization of more than two orders of magnitude on the mechanical creep data. Such quantification allows us to estimate the strain weakening in the crust. Furthermore, we introduce an additional quartz flow law for the smaller grain size applicable to rheological modelling and a better understanding of shear zone processes.

2. Starting material and sample preparation for deformation

We used pure ($>99\%$ silica), highly dense (without any visible porosity), fine-grained white Arkansas novaculite as starting material (Fig. 1). The sample orientation for the microstructural characterization of the starting material is the same as the cylindrical cores prepared for deformation experiments. All the cylindrical samples of 8 mm diameter were core-drilled from the starting material and dried at 110°C for one day. In most cases, the central locations of samples that experienced the highest strain were analysed. We also checked the top part of the samples, located closest to the upper alumina piston, where far less strain was acquired. The thick sections were

130 mechanically polished with the diamond paste of decreasing grain size (9, 3, 1, 0.25 μm), at least 10
131 minutes for each step. Once good surface conditions were achieved, final polishing with colloidal
132 silica (0.04 μm) was carried out for 20 minutes. Microstructural and chemical analysis were
133 performed from polished sections parallel to the long axis of the cores, using Scanning electron
134 microscopy (SEM), Electron backscatter diffraction (EBSD), Electron probe micro-analyzer (EPMA)
135 equipped with a cathodoluminescence (CL) detector and Secondary-ion mass spectrometry (SIMS).
136 Please see supplementary text for more details.

137 The initial microstructure is very homogeneous, consisting of grains with straight grain
138 boundaries and triple grain junctions indicating an equilibrium microstructure (Fig. 1a-c). A few
139 sporadically distributed large quartz clasts up to $\sim 100 \mu\text{m}$ in size are detected (Fig. 1a). The
140 hyperspectral cathodoluminescence (CL) image (see supplementary text) shows largely yellow
141 luminescence. The CL spectra shows a very prominent peak at 650 nm (Fig. 1d). Electron backscatter
142 diffraction (EBSD) map (see supplementary text) shows that most of the grains are strain-free, i.e.,
143 without any internal misorientation (Fig. 1e). Only a few larger grains show some degree of
144 intragranular misorientation, giving rise to the development of low-angle boundaries. The
145 crystallographic preferred orientation (CPO) of quartz considering the mean orientation of *c*-axes
146 (Fig. 1f) confirms an initial random orientation. The bulk axial ratio $b/a = 0.825$ (long axis = *a*, short
147 axis = *b*; Fig. 1f) indicates that the bulk shape of the grains is not equiaxed. The PAROR rose
148 diagram (see supplementary text) shows that there is a shape preferred orientation (SPO) parallel to
149 the cylindrical long axis (Fig. 1g). EBSD measurements of the mean 2D equivalent-diameter grain
150 size is 3.80 μm (Fig. 1h). Although limited by the step size (0.2 μm) for lower values, such a 2D
151 grain size of novaculite samples was also recorded in earlier studies (Fukuda et al., 2019; Kronenberg
152 and Tullis, 1984; Tullis and Yund, 1982). The 3D grain size analysis (see supplementary text) shows
153 a typical unimodal bell-shaped distribution with 3D mode of 5.70 μm (Fig. 1h). This value should be
154 considered as the representative grain size. Minor secondary phases include mica and rutile, the
155 former one being the source of additional H_2O and Al during the deformation (Supplementary Fig. 1).
156 Point analysis ($10 \times 10 \mu\text{m}$ area) data by SIMS (see supplementary text) indicate that initial average
157 H_2O content in quartz is 1270 H/ 10^6Si (measurements vary from 766 to 1954 H/ 10^6Si).

158 Four cylindrical samples were prepared for load-stepping experiments in the new generation
159 solid-medium (NaCl) Griggs apparatus (Orléans, France, Précigout et al., 2018) at a constant
160 temperature of 900 $^\circ\text{C}$ and a confining pressure of 1 GPa (Fig. 2a, b). The ‘as-is’ sample (OR107)
161 was prepared without adding water after drying at 110 $^\circ\text{C}$ for one day before weld-sealing the jacket
162 (Fig. 2b). In the ‘ H_2O -added’ sample (OR105), 0.1 wt.% of distilled water was added after drying at
163 110 $^\circ\text{C}$ for one day. The ‘dry’ sample (OR113) was prepared by drying novaculite at 300 $^\circ\text{C}$ for one
164 day under atmospheric conditions. We also prepared a ‘super-dry’ sample (OR116) by drying it at
165 1000 $^\circ\text{C}$ for one day. In the ‘dry’ sample, we expect much of the adsorbed H_2O at surfaces to be
166 removed in comparison to the ‘as-is’ sample, while H_2O at grain boundaries or within the crystal
167 structure of quartz, or in the micas, remains intact. In contrast, the ‘super-dry’ sample is expected to
168 have most of the H_2O removed from grain boundaries and crystal lattice in comparison to the
169 undeformed novaculite (later, SIMS analysis also confirm this), in addition to decomposition of
170 micas. One temperature-stepping experiment (OR111) was performed between 900 $^\circ\text{C}$ and 750 $^\circ\text{C}$ at
171 constant load with the ‘as-is’ novaculite (Fig. 2c). The final microstructures from these stepping
172 experiments are the result of complex $\sigma - \dot{\epsilon}$ history that the sample experienced at different steps.
173 Therefore, we carried out two additional constant- $\dot{\epsilon}$ ($\sim 10^{-6} \text{ s}^{-1}$) H_2O -added and as-is experiments
174 (689, 691) in a first-generation Tullis-modified Griggs apparatus (see Supplementary text) under the
175 same P-T conditions

(Fig. 2d) with slightly higher total strain than their counterpart load-stepping experiments for representative microstructural analysis corresponding to a constant $\dot{\epsilon}$.

3. Results

3.1. Mechanical data

All our mechanical data were processed using a MATLAB program adapted by J. Précigout (www.jacques-precigout.fr). The shortening of the samples was determined from the instrument record considering the subsequent sample lengths at any given moment during the experiments. To calculate the $\dot{\epsilon}$ out of load-stepping experiments (Fig. 2b), a straight line was fitted through the last part of the strain-time curve corresponding to the steady state condition (cf. Ghosh et al., 2022). Average σ -values (i.e., load/area) for each step were obtained from the steady-state portion of the mechanical record after correction of sample shortening and rig stiffness. Differential stress was calculated as $\Delta\sigma = \sigma_1 - \sigma_3$, based on the definition of the conventional hit point (Holyoke and Kronenberg, 2013). As expected, strain increases faster with increasing load on the sample (supplementary Fig. 2) and the slopes of the strain-time curves need some time to attain a steady state condition. At the highest T -step of the constant-load experiments (Fig. 2c), the overall slope of the strain curve is slightly convex, while it becomes slightly concave at the lowest T . The σ values also decreased slightly (~ 10 MPa) with time as a consequence of the increase in the surface area of the deformed sample (as the load is constant). Depending on the number of steps and $\dot{\epsilon}$ at each step, the bulk strain in our experiments ranges up to a maximum value of $\sim 21.3\%$. Experimental conditions and the corresponding results are sequentially shown in Table 1.

During the constant- $\dot{\epsilon}$ experiments, stress-strain curves were generated for the as-is and 0.1% H₂O-added samples that exhibits same mechanical behavior (Fig. 2d). After reaching the peak-stress, both stress-strain curves show slight weakening. The difference in flow stresses between the as-is and H₂O-added sample is within the expected variation of individual samples given an error of ± 30 MPa for the Tullis-modified Griggs-type apparatus (Holyoke and Kronenberg 2010).

3.2. Determination of n and Q .

σ and $\dot{\epsilon}$ for the load-stepping experiments were plotted in a log-log space to calculate the n -value (Fig. 2e). The slope of the power-law-fit indicates n -values of ~ 1.91 for H₂O-added, ~ 1.94 for dry and ~ 2.18 for the as-is sample. However, if we do not consider the lowest stress point for the as-is experiment, then the n value becomes ~ 1.99 . A similar issue with the lowest stress data was noted earlier (Ghosh et al., 2022). Given the ± 30 MPa accuracy of the solid-medium apparatus (Holyoke and Kronenberg, 2010), it is possible that such low stress values are less reliable. The T -stepping data are plotted in the Arrhenius $\ln(\dot{\epsilon}) - T^{-1}$ space (Fig. 2f). $Q = 118$ kJ/mol was determined from the slope of the global fit in the Arrhenius space, independent of the n -value. The n and Q values measured from the novaculites are similar to those obtained from the coarse-grained Tana quartzite (Ghosh et al., 2022).

3.3. Microstructural observations.

The misorientation images from the two constant- $\dot{\epsilon}$ samples show the formation of distorted crystal structures in the quartz grains, giving rise to the development of low-angle inner boundaries (marked in pink) and discrete sub-grain boundaries (marked in green) (Fig. 3a, b). The grain size distribution (GSD) remained ‘broadly’ unimodal with slight increase in $d_{3D}(\text{mode})$ (Fig. 3c) in comparison to the pre-deformed value (Table 1). Interestingly, the original SPO (Fig. 1h) has been replaced in the deformed samples and the grains tend to align with their long axis perpendicular to the compression direction (Fig. 3c). The lower values of the bulk axial ratio ($b/a \approx 0.65$) compared to the

219 pre-deformed value (Fig. 1h) suggest that the grains were flattened. The corresponding CPO strengths
220 remains weak without any significant CPO pattern development (Fig. 3c). Both constant- $\dot{\epsilon}$ samples
221 reveal a comparable microstructure in CL and element maps. Three types of domains are visible and
222 distributed in a patchy way: (i) domains with aggregates of CL-yellow grains, (ii) domains where CL-
223 yellow grains are less abundant, and grains with CL-yellow cores surrounded by a CL-dark
224 luminescence, and (iii) domains where grains with CL-yellow cores surrounded by a CL-blue
225 luminescence. The CL-yellow grains have on average a lower Al^{3+} content than domains with CL-
226 blue and CL-dark luminescence (Fig. 3a, b). The CL blue and dark zones visually contain slightly
227 coarser grains than the CL-yellow zones. From the EBSD maps of the load-stepping samples
228 (supplementary Fig. 5a-e), the as-is and dry samples revealed that some areas patchily show grain
229 coarsening in contrast to the H_2O -added sample with more or less homogeneous GSD (supplementary
230 Fig. 5f-h). In Fig. 4 and Supplementary Fig. 4, the corresponding backscattered electron (BSE), CL,
231 and element maps from the load-stepping samples are shown. The as-is and dry samples showed
232 regions of grain coarsening, which correspond to different orders of blue luminescence (darker to
233 brighter) with a similar spectral pattern (Fig. 5). In contrast, the areas retaining finer grains typically
234 show yellow luminescence. A closer inspection reveals that some of the coarser grains contain a
235 yellow core surrounded by a darker shell, which progressively becomes brighter blue towards the
236 grain boundary. In contrast to these samples, the H_2O -added deformed sample show more
237 homogeneously developed core-shell structures. The individual core-shell structures are not always
238 symmetric with respect to the grain boundaries and cores possess a sharp polygonal shape
239 (Supplementary Fig. 4b). A similar homogeneously-developed core-shell can be observed in the H_2O -
240 added constant- $\dot{\epsilon}$ sample (689), but from a different location (Supplementary Fig. 6).

241 The CL spectra corresponding to three different luminescence that constitutes a core-
242 shell structure in the H_2O -added sample is shown (Fig. 5, 6a). The brighter blue silica material
243 shows a similar spectral pattern as the darker blue shell, but the two prominent wavelength peaks
244 between 350 to 475 nm are more intense for the brighter blue shell. On the contrary, the yellow
245 core shows a similar pattern as the undeformed novaculite (Fig. 1d) with a very strong peak at 650
246 nm. It is clear from the element line profile that the yellow cores become brighter blue as the Al^{3+}
247 content increases from the core to the boundary (Fig. 6a). The grain boundary regions are highlighted
248 by elements such as Al, Ca, K and Na (Fig. 6b, Supplementary Fig. 4h) and a positive correlation is
249 found between the Al^{3+} versus Na^+ and K^+ from the line profiles within the quartz grains (Fig. 6c).
250 SIMS point analysis data from all the samples indicate a positive correlation between $\text{H}/10^6\text{Si}$ and
251 $\text{Al}/10^6\text{Si}$ (Fig. 6d). Both the as-is and H_2O -added samples do not show significant differences in
252 terms of grain-scale H_2O content. The lowest values of point analysis data from the interiors of
253 the deformed grain should overlap the values measured from undeformed quartz aggregate.
254 However, due to large spot size ($\sim 10\ \mu\text{m}$) the grain interior values have some contribution from the
255 shells. Interestingly, the as-is quartz aggregate contains a much higher amount of H^+ than the
256 source novaculite, indicating additional amount of H_2O released from the micas during
257 deformation. SIMS point analysis data indicate low average H_2O contents of 454 $\text{H}/10^6\text{Si}$ (varies
258 from 399 to 472 $\text{H}/10^6\text{Si}$) in the super-dry sample.

259 The BSE and band contrast images from the deformed samples commonly show many grains
260 with straight boundaries and triple (some quadruple) junctions and new porosity development
261 along those junctions and grain boundaries (Figs. 4a, d, g, 6 e-g). Some of the small pore spaces show
262 high Al-contents in the WDS maps (Fig. 4a, c). Such red spots often are exaggerated in size
263 as a consequence of analytical resolution. However, the pore spaces and boundaries can act as
264 reservoirs for the fluid and the elements dissolved in it. It is noteworthy that a few grain
265 boundaries from the

264 H₂O-added sample (Fig. 6e) are curved (marked by a green arrow) in the BSEmaps. This feature is
265 typically observed in natural samples with grain boundary migration (GBM) (Stipp et al., 2004).

266 The core-shell structure indicates that there was a progressive reconstitution of silica material
267 from the core to the boundary, which can be detected by CL. It is well known that the top part of the
268 deformed samples, closest to the alumina piston, acquires far less strain than the central part.
269 The EBSD map shows evidence of minor internal crystal-plastic deformation and the development
270 of a weak SPO (Fig. 7c). Additionally, it is clear that far less grain boundary reconstitution and
271 porosity development (Fig. 7a, b) had occurred in comparison to the microstructures in the more
272 deformed parts. The ‘super-dry’ sample is too strong to be deformed under differential stresses (as
273 high as > 900 MPa) below the confining pressure. It is also clear from the EBSD maps that there
274 is no internal crystal-plastic strain and grain sizes did not show any significant modification
275 (Supplementary Fig. 7). CL maps indicate that no grain boundary reconstitution had occurred (Fig.
276 7d).

4. Discussion

4.1. Comparison with Previous Studies.

277
278 Using the 0.1 wt. % H₂O-added coarse-grained quartzite (Tana quartzite) flow law (Ghosh et
279 al., 2022) with $n = 2$ and $Q = 110$ kJ/mol (equation 2), the $\dot{\epsilon}$ values are calculated at the σ , T , and P
280 reported (Table 1) from individual novaculite experiments. These $\dot{\epsilon}$ values (transparent circles) and
281 the red line derived from the equation 2 are shown in Figure 8a-d. The H₂O-added novaculite is ~ 3.5
282 times weaker than the as-is novaculite (Fig. 8a, b). A similar strength difference (~ 4 times) has been
283 novaculite is ~ 4.5 times weaker than the as-is Tana quartzite (Fig. 8a). The H₂O-added novaculite is
284 ~ 4 times weaker than the H₂O-added Tana (data calculated from the flow law, equation 2) at the same
285 condition (Fig. 8b). The dry and as-is novaculite samples show only slight (~ 1.4 times) differences
286 (Fig. 8c). The maximum strength difference (more than an order of magnitude) arises between the
287 end-member samples, i.e., the as-is Tana and H₂O-added novaculite, where the combined effect of
288 grain size and addition of H₂O accumulates. The activation energy for as-is novaculite calculated from
289 the Arrhenius $\ln(\dot{\epsilon}) - T^{-1}$ space is very similar to the values calculated from the Tana quartzite (Fig.
290 8d). Thus, the slope of the creep data (log-log and Arrhenius space) indicative of $n (= 2)$ and $Q (= 110$
291 kJ/mol) values does not change between the novaculite (as-is, H₂O-added, and dry) and Tana samples
292 (as-is and H₂O-added) within the error associated with the Griggs apparatus. Therefore, the strength
293 difference between these experiments is best expressed by the different A -values of the flow law (see
294 supplementary text). For example, multiplication of the A -value (equation 2) with 3.5 predicts the
295 strength of the 0.1 wt. % of H₂O-added novaculite.
296

297 In Figure 8e, the original mechanical data (σ and $\dot{\epsilon}$) were normalized to the non-dimensional
298 stress (σ_0) and strain rate ($\dot{\epsilon}_0$) ratios in reference to the coarse-grained Tana flow law (equation 2). In
299 this way, we can compare the results from earlier constant- $\dot{\epsilon}$ experiments using the novaculite and
300 coarse-grained quartzite, where mechanical data were obtained from a variety of σ , $\dot{\epsilon}$, T , and P
301 conditions (Ghosh et al., 2021; Yabe et al., 2020). Only the results from previous studies that satisfied
302 the Goetze’s criterion were used to avoid any contribution from the brittle deformation mechanisms.
303 The original mechanical data (σ and $\dot{\epsilon}$) published earlier was normalized to non-dimensional stress
304 (σ_0) and strain rate ($\dot{\epsilon}_0$) ratios as $\sigma_0 = \frac{\sigma}{\sigma_{ref}}$ and $\dot{\epsilon}_0 = \frac{\dot{\epsilon}}{\dot{\epsilon}_{ref}}$. Here, the reference strain rate ($\dot{\epsilon}^{*ref}$) was
305 calculated from the Tana flow law (equation 2) by substituting the T with temperature-values at which
306 each original mechanical data was acquired and the stress term (σ) with the σ^{*ref} . A fixed value of
307 100 MPa as σ^{*ref} was used in this calculation. The strength differences between the Tana quartzite

308 and novaculites remain the same as those described in the previous section. Irrespective of the total
1 309 strain, all the co-axial experimental data (as-is to H₂O-added) from earlier natural coarse-grained
2 310 samples are plotted in the shaded region (cf. Ghosh et al., 2022). The as-is novaculite deformed at
3 311 700-850 °C and 1 GPa (Bishop, 1996) followed our as-is novaculite results at higher σ and $\dot{\epsilon}$. H₂O-
4 312 added (0.03 to 0.4 wt. %) novaculite deformed at 800 and 850 °C (Kronenberg and Tullis, 1984) plot
5 313 between our as-is and H₂O-added novaculite data demonstrating a good reproducibility for similar
6 314 starting material. These observations confirm the capability of the coarse-grained Tana flow law
7 315 (equation 2) to express the original mechanical data in a predicted manner from previous studies
8 316 using novaculite, given a ± 30 MPa error generally associated with the Tullis-modified Griggs-type
9 317 apparatus (Holyoke and Kronenberg, 2010). It is not surprising that the 0.2 wt. % H₂O-added mixture
10 318 of coarse- and fine-grained quartz aggregate made from pulverized dry single crystal of quartz
11 319 (Richter et al., 2018) is following the trend of our as-is novaculite and H₂O-added Tana quartzite data,
12 320 but at higher σ and $\dot{\epsilon}$. Richter et al. (2018) also documented $n = 1.8$, which again confirms that the n -
13 321 value is rather grain-size-insensitive. Furthermore, the data from the coarse-grained (~ 100 μm) Black
14 322 Hills quartzite (Heilbronner and Kilian, 2017; Kidder et al., 2016; Stipp et al., 2006) fall between our
15 323 end-member data, that is as-is Tana and H₂O-added novaculite. The mechanical data from these
16 324 studies were chosen as they clearly document significant recrystallization. Mechanical data from fine-
17 325 grained quartz-sand power (Fukuda et al., 2018), using the Tullis-modified Griggs apparatus forms
18 326 the upper boundary of the shaded region in the nondimensional plot. Interestingly, they also recorded
19 327 a n -value close to 2 (~ 1.8). These data are weaker than our H₂O-added novaculite, although the
20 328 difference is not large. This may reflect the inherent variability between starting materials. Although,
21 329 Rutter and Brodie, (2004b) reported grain-size-sensitive diffusion creep ($n = 1$) from extremely fine-
22 330 grained quartz aggregates, their data broadly overlap our data. This is surprising, given that GSS
23 331 creep is supposed to significantly weaken the samples. Nonetheless, our novaculite results support
24 332 their conclusion that diffusion creep does not dominate quartz at a grain size > 1 μm under the
25 333 laboratory $\dot{\epsilon}$.

334 4.2. CL-blue luminescence and substitution of Si⁴⁺

335 Substitution of Si⁴⁺ by Al³⁺ is common in natural quartz, and leads to the joint
336 incorporation of monovalent ions in the crystal structure for charge balance (Yuan et al., 2023).
337 The CL-blue luminescence in quartz was shown earlier to contain high concentrations of Al³⁺
338 (Raimbourg et al., 2021) from natural samples. In the present study, the blue (dark to bright)
339 CL signal from the deformed novaculites is also strongly correlated with Al³⁺. On the other hand, if
340 Ti⁴⁺ is present in the system, it can be also responsible for a blue luminescence (Bestmann and
341 Pennacchioni, 2015). In the deformed novaculites, Ti⁴⁺ is present in very low concentration and
342 found to be correlating with H⁺ (see Supplementary text), but the corresponding CL-wavelength
343 with a maximum at ~ 415 nm (Bestmann and Pennacchioni, 2015) is missing. Thus, it appears
344 that Al³⁺ is responsible for the CL-blue spectra in our samples (Fig. 5), but future studies are needed
345 to evaluate the effect of Ti⁴⁺ as it is also available in the novaculites. We found that Al³⁺ has a
346 positive correlation with the monovalent cations (Na⁺, K⁺, H⁺) for charge balance (Fig. 6c, d). It is
347 likely that the grain boundaries together with opening and closing of pores (Fusseis et al., 2009)
348 acted as fluid pathways for the transport of dissolved elements that may originate from impurities
349 (e.g., micas) present in the novaculite. The Na+K/Al atomic ratios vary up to 0.56 and the charge
350 deficit possibly is compensated by the intake of H⁺ (Perny et al., 1992). However, Al/H atomic
351 proportion is of the order 0.5, which indicate H⁺ is incorporated in larger proportion than what is
352 needed for charge compensation. The high H⁺ content might result from submicron size inclusions
353 or H₂O present in the grain boundaries. Noticeably, the variation in the Al³⁺ content does not always
354 correlate systematically with darker or brighter blue CL-luminescence (Fig. 6a). It is possible that
355 charge-compensating ions are playing a critical role as the CL-activator (Fig. 5); the ions with larger
356 atomic radius will distort the crystal lattice in comparison to

355 the smaller ions (Yuan et al., 2023). The role of the individual charge-compensating cations on the CL
356 signal is difficult to determine and needs further studies.

357 **4.3. Deformation mechanisms related to grain boundary processes**

358 The core-shell-structure observed under the CL implies a reconstitution process where
359 the unaltered yellow core of the original grains is preserved and surrounded by reconstituted
360 silica material that has exchanged elements while forming the shell. In the presence of an
361 aqueous fluid along the grain boundaries, a GBM process takes place through dissolution-
362 precipitation between adjacent grains (Fig. 9) (Pearce and Wheeler, 2010; Poirier and Guillopé, 1979;
363 Urai et al., 1986). We can reasonably predict that the cations (Al^{3+} , Na^+ , K^+ , Ca^{2+} , H^+) present in
364 the system can move by diffusion in the grain boundary fluid and that diffusion in the fluid is
365 sufficiently fast to account for the concentration observed at the grain boundaries (Fig. 6b). Al^{3+} is
366 incorporated into the quartz via exchange by the migrating grain boundaries, and the outer shell
367 acquires a higher concentration of Al^{3+} and other monovalent cations required for charge balance
368 (Fig. 6a). The volume of the altered composition (blue or dark shell) marks the local extent of
369 the GBM process. A potential Al self-diffusion in SiO_2 is too slow to produce the width of the Al-
370 enriched outer rims we observed (Tailby et al., 2018).

371 Our microstructural observations, such as the formation of pores, triple and
372 quadruple junctions, straight boundaries, and the development of strong SPO along with change
373 in shape of individual grains without any significant CPO (Fig. 3), are consistent with GBS-
374 related processes observed in natural and experimentally deformed samples (Dimanov et al., 2007;
375 Fuisseis et al., 2009; Menegon et al., 2015; Rybacki et al., 2003; White et al., 1980). The
376 efficiency of GBS can be increased by dissolution-precipitation in the following two ways: (1)
377 GBM through dissolution-precipitation can modify the geometry of the grain boundary interfaces
378 and orient the neighbouring grains plastically compatible for sliding (shape change). (2) The
379 surface asperities (e.g., non-planar boundaries) can be removed by preferential dissolution and
380 transfer of silica material over a short diffusion distance (nm scale) along the grain boundary
381 interfaces, before precipitation (cf. Ashby, 1972; Raj and Ashby, 1971). In metals GBS and GBM
382 can be found to be coupled and sequential processes (Wilkinson and Cáceres, 1984). The fluid
383 present along grain boundaries and pores can disperse as a result of local grain-scale pressure
384 gradients resulting from the opening and closing of pores by GBS (Fuisseis et al., 2009) (Fig. 9).
385 Therefore, an interrelationship between the efficiency of GBS, GBM through dissolution-
386 precipitation, local grain-scale stresses, and the availability of H_2O at grain boundaries can be
387 expected. However, it is difficult to ascertain whether the pores were immediately filled by
388 precipitating material or remained open for a certain duration of time, as we still do not fully
389 understand the interdependence of these processes well enough. It is likely that the progressive
390 weakening observed in novaculites or in Tana from dry to H_2O -added conditions (Fig. 8) can be
391 correlated with a progressive increase in the effect of GBS throughout the samples. The
392 efficiency of GBS should also be increased with decreasing grain size (Langdon, 2006) as more grain
393 boundary surface becomes available for dissolution-precipitation. The strength difference
394 between Tana and novaculite samples can be explained in this way (Fig. 7). If we consider the CL-
395 blue colours and pervasive porosity development in the H_2O -added sample (Fig. 4a, b) as a
396 proxy to the GBS mechanism facilitated by the dissolution-precipitation and GBM, then it is
397 visibly clear that the CL-yellow patches in the as-is sample (Fig. 4d, e) and the top part of all the
398 deformed samples (Fig. 7a) experienced less GBM and porosity development (Fig. 4a,
399 Supplementary Fig. 7). It is probable that the initial water distribution controls the areas of grain
400 coarsening in the as-is sample, and explains why the H_2O -added sample reach a more homogeneous
401 GSD.

400 In the H₂O-added sample, the remaining yellow cores were of different sizes,
1 401 asymmetric, and, in many cases, the whole grain may have been reconstituted (Fig. 4b). This
2 402 observation implies that the present position of the boundaries between the yellow and dark/blue
3 403 rims is not necessarily identical to the original grain boundary of the undeformed novaculite and
4 404 suggests that the grain boundaries can also migrate inward and reconstitute at least parts of the
5 405 grain interior. Multiple migration or sweeping of boundaries might be needed to
6 406 substantially change the element concentration (Hay and Evans, 1987a; Negrini et al., 2014;
7 407 Pearce and Wheeler, 2010) from the grain boundary to the interior (Fig. 7a). Hay and Evans, (1987a,
8 408 1987b) described boundaries that migrated back and forth in response to the difference in chemical
9 409 potential (the exact mechanism is unknown) and change the composition of calcite grains repeatedly
10 410 by a process called chemically-induced grain boundary migration (CIGBM). Conversely, grain
11 411 boundaries can sweep and reconstitute whole grains (Fig. 6a, e), as in strain-induced grain
12 412 boundary migration (SIGBM) (Guillope and Poirier, 1979; Poirier and Guillopé, 1979). The
13 413 potential energy that drives the SIGBM arises from the local difference in dislocation density.
14 414 It is conceivable that the original grains (CL-yellow) have had a higher dislocation density than
15 415 the reconstituted blue material and GBM (Fig. 6e) act as a recovery mechanism during
16 416 deformation (Fig. 9). It has been argued that the internal distortion, thus, the dislocation density
17 417 is greater in ice grains poorly oriented for easy slip. Such grains are consumed by neighbouring
18 418 grains (suitably oriented for easy slip) with lower the dislocation density via GBM (Qi et al.,
19 419 2017). SIGBM in a strict sense takes place without a change in chemical composition.
20 420 Although, the low-angle (inner, sub-grain) boundaries observed in EBSD maps can act as
21 421 pathways for ions. Previously, a comparable core-shell structure was numerically modelled for a
22 422 plagioclase aggregate assuming a surface energy-driven GBM mechanism under hydrostatic stress
23 423 hydrostatic grain growth (Fig. 7i in Fukuda et al., 2019) and natural quartzite experiencing static
24 424 annealing (Piazolo et al., 2005). Even though driving potentials can be different (surface *versus* strain
25 425 energy), it is reasonable to assume that similar GBM processes operate during both creep and
26 426 static grain growth. The chemical change of Al³⁺ substitution in quartz is very small; therefore, it is
27 427 possible that SIGBM may provide the main driving potential for GBM (silica to dissolve in the grain
28 428 boundary fluid) (Fig. 9), but contributions from CIGBM and surface energy cannot be ruled out.

37
38 429 Surprisingly, the addition of 0.1 wt.% H₂O induces a similar order of weakening in both Tana
39 430 or novaculite samples (Fig. 8), although the grain boundary surface density is ~55 times higher in
40 431 novaculite compared to Tana (considering the equivalent cube). It seems that it is not the amount of
41 432 H₂O that is present in the grain boundaries and enters the crystal is affecting the strength (Kronenberg
42 433 et al., 2020), and the original natural samples contain sufficient grain-scale H₂O for plastic
43 434 deformation. Instead, it appears critical how much grain boundary surface area in the whole sample
44 435 becomes reconstituted with available H₂O, contributing to the H₂O weakening (dry versus as-is
45 436 versus H₂O-added). This conclusion is supported by the fact that the SIMS analysis of grain-scale
46 437 H₂O count of the deformed quartz aggregate (Fig. 6d) did not show any significant variations between
47 438 the as-is and H₂O-added samples, although they show a difference in mechanical strength (Fig. 2d).
48 439 However, in the H₂O-added experiment (Fig. 4b), as much as 90% of the image area became
49 440 reconstituted (i.e., CL-blue) in ~27 hours. In comparison, the as-is and dry samples that were
50 441 deformed for more than six days showed less than 50% reconstitution (Fig. 4). Therefore, grain
51 442 coarsening, reconstitution of SiO₂, dispersion of H₂O, and the development of porosity are linked. In
52 443 the absence of H₂O (Fig. 6d) along the grain boundaries, the interrelationship between the
53 444 dissolution-precipitation (GBM) and GBS has not been possible in the super-dry sample (Fig. 8),
54 445 where the grain interiors are also too dry to show any evidence of plastic deformation (Griggs and
55 446 Blacic, 1965) (Fig. 8, Supplementary Fig. 7). The limit, in terms of H₂O content, between deformable
56 447 quartz material and the undeformable one, is between ~500 and ~750 H/10⁶Si (Fig. 6d) (i.e., the
57
58
59
60
61
62
63
64
65

448 and the lowest value of the undeformed novaculite). At laboratory strain rates and temperatures,
1 449 similar range of water content values were also earlier reported for the absence of brittle deformation
2 450 and fully crystal plastic deformation (Poirier, 1985; Kronenberg, 1994; Stünitz et al., 2017).

4 451 **4.4. A grain-size-insensitivity quartz flow law linked to the microphysics.**

6 452 The fact that both the n and Q values of fine-grained novaculite are very similar to those of
7 453 coarse-grained Tana quartzite irrespective of the H₂O content suggests that the n and Q values are
8 454 grain-size-independent and that the same combination of deformation processes is active in
9 455 experiments above a grain size of (d_{2D}) $\sim 4 \mu\text{m}$ ($d_{3D} \sim 6 \mu\text{m}$). From EBSD mapping, it is evident that
11 456 plastic strain (internal misorientations accompanied by the development of low angle inner and sub-
12 457 grain boundaries) in the novaculite is achieved by crystal-plastic processes (Figs. 3, 4; Supplementary
13 458 Fig. 3 a-c). It has been demonstrated that the bulk strain in Tana quartzite was achieved by
14 459 intracrystalline deformation (Nègre et al., 2021). However, strain incompatibilities arising from an
15 460 insufficient number of independent slip systems, and plastic anisotropy among neighbouring grains do
16 461 not allow for homogeneous deformation (Hutchinson, 1976), even if individual grains become weaker
17 462 by the infiltration of H₂O (Griggs and Blacic, 1965). Both, GBM and GBS may act as processes to
18 463 remove such incompatibilities as accommodation mechanisms irrespective of the grain size to prevent
19 464 hardening during dislocation glide. As explained in the above section, the strength difference between
20 465 the Tana and novaculite samples can be explained by how much grain boundary area is available to
21 466 become reconstituted by GBM through dissolution-precipitation and for GBS. Similar grain boundary
22 467 accommodation mechanisms have been invoked to explain plasticity over a large grain size range in
23 468 wet ice (Goldsby, 2006), halite (Bourcier et al., 2013), and in olivine (Hansen et al., 2011; Samae et
24 469 al., 2021). As illustrated in earlier studies, GBM can also act as a recovery mechanism in addition to
25 470 sub-grain formation during dynamic recrystallization in highly strained samples (Nègre et al., 2021).
26 471 Diffusion of H₂O in quartz is very slow at an experimental time-scale (Kronenberg et al., 1986;
27 472 Gerretsen et al., 1989) and H₂O transfer by microcracking in grains and grain boundary regions has
28 473 been invoked for H₂O infiltration (FitzGerald et al. 1991; Stünitz et al., 2017). Our SIMS analyses
29 474 indicate that GBM through dissolution-precipitation is another potential mechanism that allows H₂O
30 475 to enter the quartz crystal. Moreover, it is known that the dissolution-precipitation process is pressure
31 476 dependent (Manning, 1994, 2018) so that polycrystalline quartz becomes weaker with increasing
32 477 confining pressure (Kronenberg and Tullis 1984; Holyoke and Kronenberg 2013; Nègre et al., 2021).
33 478

41 479 Although grain size has an effect on the material strength (Tana versus novaculite), as the
42 480 slope of the creep data (log-log and Arrhenius space) did not change for a considerable grain size
43 481 range, it appears more practical to use different A -values to express the differences in strength as a
44 482 proxy to the efficiency of the GBS mechanism. For example, the A -value for the ‘as-is’ coarsegrained
45 483 Tana sample ($d_{2D(\text{mean})} = \sim 200 \mu\text{m}$) will be ~ 4 times lower than the A -value reported for the H₂O-
46 484 added Tana quartzite ($= 1.56 \times 10^{-9}/\text{MPa/s}$) in equation 2. The A -value for a material similar to the
47 485 as-is novaculite sample is the same as the A -value ($= 1.56 \times 10^{-9}/\text{MPa/s}$) reported for the H₂O-
48 486 added Tana. The A -value for a material similar to the H₂O-added novaculite sample ($d_{2D(\text{mean})} = \sim 4$
49 487 μm) is 4 times higher than the A -value for the H₂O-added Tana. Then, by simple linear
50 488 approximation, the A -value for a H₂O-added quartz aggregate with a grain size of $\sim 98 \mu\text{m}$ will be two
51 489 times higher than the reported value in the equation 2. Alternatively, one may use the grain size
52 490 exponent of 0.51 ± 0.13 from Fukuda et al., (2018).

58 491 **4.5. How can the continental crust be weakened in order to facilitate shear localization?**

492 Considering all differences in H₂O content and grain size, a maximum strength difference of
1 493 about one order of magnitude is observed between the as-is Tana and H₂O-added novaculite (Fig. 8e).
2 494 It suggests that a typical quartz-bearing crustal rock can be significantly softened by GSR
3 495 (e.g., dynamic recrystallization) if there is an adequate amount of H₂O present to saturate the
4 496 grain boundaries in the recrystallized fraction. Earlier the direct relationship between
5 497 recrystallization processes and H₂O weakening in quartz has been inferred (Tullis and Yund,
6 498 1989). Therefore, the liberation of H₂O from the hydrous phases and from primary crystals by
7 499 recrystallization (Fukuda et al., 2023) to the grain boundaries can be an effective strain
8 500 localization method in nature and may start positive feedback in the shear zone (Finch et al., 2016).
9 501 However, without a H₂O source or H₂O loss (Kronenberg et al., 2020) during deformation from the
10 502 shear zone, only a modest weakening (~5 times) is expected (Fig. 7).

14 503 The original mechanical data (σ and $\dot{\epsilon}$) reported in earlier constant- $\dot{\epsilon}$ experiments (Fig. 8e) are
15 504 measured from the peak stress or the steady state (after reaching peak stress) portion of the stress-
16 505 strain curve. This means that the peak strength of the quartz aggregates (fine or coarse) can be
17 506 reasonably predicted by our flow law (shaded region in Fig. 8e). However, a number of experiments
18 507 show weakening in the stress-strain curve after the peak stress, for example, the typical regime 1
19 508 stress-strain curves (700 °C, 1.5 GPa and $\dot{\epsilon} = 10^{-6} \text{ s}^{-1}$) from coarse-grained quartzite (Hirth and Tullis,
20 509 1992). The progressive weakening has been inferred to be a consequence of increasing amounts of
21 510 dynamic recrystallization (bulges) along grain boundaries (Hirth and Tullis, 1992). As novaculite in
22 511 this study has been chosen to represent a fully recrystallized (and recovered) material compared to a
23 512 coarse-grained starting material, the maximum weakening at 100% recrystallization in the quartzite
24 513 should be limited by the novaculite mechanical data, as observed in Fig. 8e. However, it appears that
25 514 even with 20-30 % of recrystallization (> 45-55 % strain), the quartzite stress-strain curve comes very
26 515 close to that of the 0.17 wt.% H₂O-added novaculite curve (Fig. 3a of Hirth and Tullis, 1992). In
27 516 shear experiments (800 °C, 1 GPa and $\dot{\epsilon} = \sim 2.5 \times 10^{-4} \text{ s}^{-1}$), Richter et al., (2018) observed that bulging
28 517 recrystallization (regime 1) concentrates along shear bands. It is rational to assume that after
29 518 significant shortening, geometrical softening by the development of foliations, SPO, CPO, shear
30 519 bands, micro shear zones, etc. in the co-axial experiments are likely (Nègre et al., 2021; Pongrac et
31 520 al., 2022). Therefore, the weakening observed in regime 1 of Hirth and Tullis, (1992) and in other
32 521 experiments after reaching the peak stress have a significant contribution from geometrical softening
33 522 in addition to the GSR. These results indicate that 20 to 30% of recrystallized material are sufficient
34 523 to determine the mechanical behaviour by geometric weakening (Handy, 1994). As mentioned above,
35 524 without a H₂O source the maximum weakening expected is ~5 times (Fig. 8e) the strength of the
36 525 protolith by GSR. Therefore, if it can be demonstrated that a higher order of weakening (> half an
37 526 order of magnitude) is needed for sustainable shear zone development, then factors like geometric
38 527 softening are necessary. On the other hand, if GSR as observed from natural mylonitic rocks is the
39 528 most important mechanism of strain localization, then only a modest weakening (~5 times) is required
40 529 to develop sustainable plate boundary shear zones in the quartz-rheology dominated crust.

50 530 **Conclusions**

51 531 Our constant-load experiments demonstrate that the flow law parameters (stress exponent of
52 532 $n \approx 2$ and activation energy of $Q = 110 \text{ kJ/mol}$) of polycrystalline quartz are independent of the grain
53 533 size variations (at the range of ~ 200 to $\sim 3 \mu\text{m}$). Grain size differences of this order of magnitude
54 534 are generally observed in natural rocks. Our direct observational evidence from deformed fine-
55 535 grained novaculites shows that the n -value of 2 represents a combination of serial processes involving
56 536 grain boundary migration and grain boundary sliding as accommodation processes to obliterate strain
57 537 incompatibilities resulting from dislocation glide in grain interiors. Furthermore, grain boundary

538 migration by dissolution-precipitation can locally eliminate the strain incompatibilities at the
1 539 grain boundaries and shape the grains in a way that is more suitable for grain boundary sliding. In
2 540 these ways, the grain boundary processes may prevent strain hardening. The differences in the
3 541 between coarse- and fine-grained quartz (Tana and novaculites samples, respectively) can account for
4 542 the differences in strength and grain size. The grain boundary processes in the presence of H₂O are the
5 543 main accommodating mechanism in dislocation creep of quartz aggregates. These processes leave a
6 544 chemical signature in the microstructure that can be resolved using techniques like
7 545 cathodoluminescence and chemical mapping. Furthermore, drying to the extent of the super-dry
8 546 sample suppress any sort of intra-grain plasticity, thus, the minimum amount of H₂O (472 to 766
9 547 H/10⁶Si) needed for intra-grain plasticity can be constrained.

12 548 A comparison with the mechanical properties of deformed coarse-grained Tana quartzite from
13 549 our earlier studies indicate that there will be no switch in deformation mechanisms by the grain size
14 550 reduction. Consequently, we can expect a modest weakening of ~5 times the strength of the protolith
15 551 if the grain size is reduced by dynamic recrystallization by two orders of magnitude. If a wet shear
16 552 zone material from a protolith is produced involving geometric softening (development of foliations,
17 553 SPO, CPO, shear bands, etc.), a significant weakening can be achieved. However, considering grain
18 554 size reduction as the most effective mechanism of strain localization, our results suggest that maybe a
19 555 lower amount of weakening is actually needed to make plate boundaries in the crust similar to the
20 556 Earth than previously thought.

24 557 **Acknowledgements**

26 558 The novaculite samples from Arkansas was supplied by Corbin Cannon of Arkansas
27 559 Geological Survey. The f_{H_2O} can be calculated from Tony Wither's fugacity calculator (<https://publish.uwo.ca/~awither5/fugacity/index.htm>), assuming the water pressure approximates the
28 560 confining pressure during the deformation. We thank Sylvain Janiec (ISTO) for making and partly
29 561 polishing thin sections. SG thanks Estelle Rose-Koga for her guidance during the preparation of
30 562 samples for SIMS analysis. SG, HR and LP are grateful to the LG-SIMS-Nancy team for their
31 563 technical help for SIMS measurements. We acknowledge the support from both LabEx VOLTAIRE
32 564 (LABX-100-01) and EquipEx PLANEX (ANR-11-EQPX-0036) projects. This project has benefited
33 565 from the expertise and the facilities of the Platform MACLE - CVL which was co-funded by the
34 566 European Union and Centre-Val de Loire Region (FEDER). We thank A. Dimanov and an anonymous
35 567 reviewer for their very constructive and insightful reviews that have substantially improved this
36 568 manuscript. We are also thankful to J. P. Avouac for handling this manuscript.

41 570 **References**

- 42 571
- 43 572
- 44 573 Ashby, M.F., 1972. Boundary defects, and atomistic aspects of boundary sliding and diffusional
45 574 creep. *Surf Sci* 31, 498–542.
- 46 575 Bercovici, D., Ricard, Y., 2016. Grain-damage hysteresis and plate tectonic states. *Physics of the*
47 576 *Earth and Planetary Interiors* 253, 31–47.
48 577 [https://doi.org/https://doi.org/10.1016/](https://doi.org/https://doi.org/10.1016/j.pepi.2016.01.005)
49 578 [j.pepi.2016.01.005](https://doi.org/https://doi.org/10.1016/j.pepi.2016.01.005)
- 50 579 Bestmann, M., Pennacchioni, G., 2015. Ti distribution in quartz across a heterogeneous shear
51 580 zone within a granodiorite: The effect of deformation mechanism and strain on Ti
52 581 resetting. *Lithos* 227, 37–56. <https://doi.org/10.1016/j.lithos.2015.03.009>
- 53 582 Bishop, R.R., 1996. Grain boundary migration in experimentally deformed quartz aggregates:
54 583 The relationship between dynamically recrystallized grain size and steady state flow
55 584 stress. Brown University, Providence, RI 36.
- 56 585
- 57 586
- 58 587
- 59 588
- 60 589
- 61 590
- 62 591
- 63 592
- 64 593
- 65 594

- 584 Blacic, J.D., Christie, J.M., 1984. Plasticity and hydrolytic weakening of quartz single crystals. *J*
1 585 *Geophys Res Solid Earth* 89, 4223–4239.
- 2
3 586 Coble, R.L., 1963. A model for boundary diffusion controlled creep in polycrystalline materials.
4 587 *J Appl Phys* 34, 1679–1682.
- 5
6 588 Dimanov, A., Rybacki, E., Wirth, R., Dresen, G., 2007. Creep and strain-dependent
7 589 microstructures of synthetic anorthite-diopside aggregates. *J Struct Geol* 29, 1049–1069.
8 590 <https://doi.org/10.1016/j.jsg.2007.02.010>
- 9
10 591 Finch, M.A., Weinberg, R.F., Hunter, N.J.R., 2016. Water loss and the origin of thick
11 592 ultramylonites. *Geology* 44, 599–602. <https://doi.org/10.1130/G37972.1>
- 12
13 593 Fitz Gerald, J. D., J. N. Boland, A. C. McLaren, A. Ord, and B. E. Hobbs (1991),
14 594 Microstructures in water-weakened single crystals of quartz, *J. Geophys. Res.*, 96, 2139–
15 595 2155, doi:10.1029/90JB02190
- 16
17 596 Fukuda, J. ichi, Holyoke, C.W., Kronenberg, A.K., 2018. Deformation of Fine-Grained Quartz
18 597 Aggregates by Mixed Diffusion and Dislocation Creep. *J Geophys Res Solid Earth* 123,
19 598 4676–4696. <https://doi.org/10.1029/2017JB015133>
- 20
21 599 Fukuda, J., Okudaira, T., Ohtomo, Y., 2023. Water release and homogenization by dynamic
22 600 recrystallization of quartz. *Solid Earth* 14, 409–424. [https://doi.org/10.5194/se-14-409-](https://doi.org/10.5194/se-14-409-2023)
23 601 [2023](https://doi.org/10.5194/se-14-409-2023)
- 24
25 602 Fukuda, J., Raimbourg, H., Shimizu, I., Neufeld, K., Stünitz, H., 2019. Experimental grain
26 603 growth of quartz aggregates under wet conditions and its application to deformation in
27 604 nature. *Solid Earth* 10, 621–636. <https://doi.org/10.5194/se-10-621-2019>
- 28
29 605 Fusseis, F., Regenauer-Lieb, K., Liu, J., Hough, R.M., De Carlo, F., 2009. Creep cavitation can
30 606 establish a dynamic granular fluid pump in ductile shear zones. *Nature* 459, 974–977.
31 607 <https://doi.org/10.1038/nature08051>
- 32
33 608 Ghosh, S., Koizumi, S., Hiraga, T., 2021. Diffusion Creep of Diopside. *J Geophys Res Solid*
34 609 *Earth* 126. <https://doi.org/10.1029/2020JB019855>
- 35
36 610 Ghosh, S., Stünitz, H., Raimbourg, H., Précigout, J., 2022. Quartz rheology constrained from
37 611 constant-load experiments: Consequences for the strength of the continental crust. *Earth*
38 612 *Planet Sci Lett* 117814. <https://doi.org/10.1016/j.epsl.2022.117814>
- 39
40 613 Gleason, G.C., Tullis, J., 1995. A flow law for dislocation creep of quartz aggregates determined
41 614 with the molten salt cell. *Tectonophysics* 247, 1–23.
42 615 [https://doi.org/https://doi.org/10.1016/0040-1951\(95\)00011-B](https://doi.org/https://doi.org/10.1016/0040-1951(95)00011-B)
- 43
44 616 Goldsby, D.L., 2006. Superplastic flow of ice relevant to glacier and ice- sheet mechanics.
45 617 *Glacier science and environmental change* 308–314.
- 46
47 618 Goldsby, D.L., Kohlstedt, D.L., 2001. Superplastic deformation of ice: Experimental
48 619 observations. *J Geophys Res Solid Earth* 106, 11017–11030.
49 620 <https://doi.org/10.1029/2000jb900336>
- 50
51 621 Griggs, D., 1974. A model of hydrolytic weakening in quartz. *J Geophys Res* 79, 1653–1661.
- 52
53 622 Griggs, D.T., Blacic, J.D., 1965. Quartz: Anomalous weakness of synthetic crystals. *Science*
54 623 (1979) 147, 292–295.
- 55
56
57
58
59
60
61
62
63
64
65

624 Guillope, M., Poirier, J.P., 1979. Dynamic recrystallization during creep of single-crystalline
1 625 halite: an experimental study. *J Geophys Res* 84, 5557–5567.
2 626 <https://doi.org/10.1029/JB084iB10p05557>
3

4 627 Handy, M.R., 1994. The energetics of steady state heterogeneous shear in mylonitic rock.
5 628 *Materials Science and Engineering: A* 175, 261–272.
6 629 [https://doi.org/https://doi.org/10.1016/0921-5093\(94\)91065-0](https://doi.org/https://doi.org/10.1016/0921-5093(94)91065-0)
7

8 630 Hansen, L.N., Zimmerman, M.E., Kohlstedt, D.L., 2011. Grain boundary sliding in San Carlos
9 631 olivine: Flow law parameters and crystallographic-preferred orientation. *J Geophys Res*
10 632 *Solid Earth* 116. <https://doi.org/10.1029/2011JB008220>
11

12 633 Hay, R.S., Evans, B., 1987a. Chemically induced grain boundary migration in calcite:
13 634 temperature dependence, phenomenology, and possible applications to geologic systems.
14 635 *Contributions to Mineralogy and Petrology* 97, 127–141.
15 636 <https://doi.org/10.1007/BF00375220>
16 637

17 637 Hay, R.S., Evans, B., 1987b. Chemically induced migration in low and high angle calcite grain
18 638 boundaries. *Acta metallurgica* 35, 2049–2062.
19

20 639 Heilbronner, R., Kilian, R., 2017. The grain size(s) of Black Hills Quartzite deformed in the
21 640 dislocation creep regime. *Solid Earth* 8, 1071–1093. [https://doi.org/10.5194/se-8-1071-](https://doi.org/10.5194/se-8-1071-2017)
22 641 [2017](https://doi.org/10.5194/se-8-1071-2017)
23

24 642 Herring, C., 1950. Diffusional viscosity of a polycrystalline solid. *J Appl Phys* 21, 437–445.
25

26 643 Hier-Majumder, S., Mei, S., Kohlstedt, D.L., 2005. Water weakening of clinopyroxenite in
27 644 diffusion creep. *J Geophys Res Solid Earth* 110, 1–12.
28 645 <https://doi.org/10.1029/2004JB003414>
29

30 646 Hirth, G., Kohlstedt, D., 2004. Rheology of the upper mantle and the mantle wedge: A view
31 647 from the experimentalists, in: *Geophysical Monograph Series*. Blackwell Publishing Ltd,
32 648 pp. 83–105. <https://doi.org/10.1029/138GM06>
33

34 649 Hirth, G., Teyssier, C., Dunlap, W.J., 2001. An evaluation of quartzite flow laws based on
35 650 comparisons between experimentally and naturally deformed rocks. *International Journal*
36 651 *of Earth Sciences* 90, 77–87. <https://doi.org/10.1007/s005310000152>
37

38 652 Hirth, G., Tullis, J., 1992. Dislocation creep regimes in quartz aggregates. *J Struct Geol* 14, 145–
39 653 159. [https://doi.org/https://doi.org/10.1016/0191-8141\(92\)90053-Y](https://doi.org/https://doi.org/10.1016/0191-8141(92)90053-Y)
40

41 654 Holyoke, C.W., Kronenberg, A.K., 2010. Accurate differential stress measurement using the
42 655 molten salt cell and solid salt assemblies in the Griggs apparatus with applications to
43 656 strength, piezometers and rheology. *Tectonophysics* 494, 17–31.
44 657 <https://doi.org/10.1016/j.tecto.2010.08.001>
45

46 658 Jaoul, O., Tullis, J., Kronenberg, A., 1984. EFFECT OF VARYING WATER CONTENTS ON
47 659 THE CREEP BEHAVIOR OF HEAVITREE QUARTZITE., in: *Journal of Geophysical*
48 660 *Research*. pp. 4298–4312. <https://doi.org/10.1029/jb089ib06p04298>
49

50 661 Karato, S., 2008. *Deformation of Earth Materials*. Cambridge University Press.
51 662 <https://doi.org/10.1017/CBO9780511804892>
52

53 663 Kidder, S., Hirth, G., Avouac, J.P., Behr, W., 2016. The influence of stress history on the grain
54 664 size and microstructure of experimentally deformed quartzite. *J Struct Geol* 83, 194–206.
55 665 <https://doi.org/10.1016/j.jsg.2015.12.004>
56

57
58
59
60
61
62
63
64
65

- 666 Koch, P.S., Christie, J.M., Ord, A., George, R.P., 1989. Effect of water on the rheology of
1 667 experimentally deformed quartzite. *J Geophys Res* 94.
2 668 <https://doi.org/10.1029/jb094ib10p13975>
3
- 4 669 Kronenberg, A.K., Ashley, K.T., Francis, M.K., Holyoke III, C.W., Jezek, L., Kronenberg,
5 670 J.A., Law, R.D., Thomas, J.B., 2020. Water loss during dynamic recrystallization of Moine
6 671 thrust quartzites, northwest Scotland. *Geology* 48, 557–561.
7 672 <https://doi.org/10.1130/G47041.1>
8 673
- 9 673 Kronenberg, A. K. (1994), Hydrogen speciation and chemical weakening of quartz, *Rev.*
10 674 *Mineral. Geochem.*, 29(1), 123–176.
11 675
- 12 675 Kronenberg, A.K., Tullis, J., 1984. FLOW STRENGTHS OF QUARTZ AGGREGATES:
13 676 GRAIN SIZE AND PRESSURE EFFECTS DUE TO HYDROLYTIC WEAKENING., in:
14 677 *Journal of Geophysical Research*. pp. 4281–4297.
15 678 <https://doi.org/10.1029/jb089ib06p04281>
16 679
- 17 679 Luan, F.C., Paterson, M.S., 1992. Preparation and deformation of synthetic aggregates of quartz.
18 680 *J Geophys Res* 97, 301–320. <https://doi.org/10.1029/91JB01748>
19 681
- 20 681 Menegon, L., Fusseis, F., Stünitz, H., Xiao, X., 2015. Creep cavitation bands control porosity
21 682 and fluid flow in lower crustal shear zones. *Geology* 43, 227–230.
22 683 <https://doi.org/10.1130/G36307.1>
23 684
- 24 684 Nabbarro, F.R.N., 1948. Deformation of crystals by motion of single ions, in: *Report on a*
25 685 *Conference on the Strength of Solids*. The Physical Society.
26 686
- 27 686 Nègre, L., Stünitz, H., Raimbourg, H., Lee, A., Précigout, J., Pongrac, P., Jeřábek, P., 2021.
28 687 Effect of pressure on the deformation of quartz aggregates in the presence of H₂O. *J Struct*
29 688 *Geol* 148. <https://doi.org/10.1016/j.jsg.2021.104351>
30 689
- 31 689 Negrini, M., Stunitz, H., Berger, A., Morales, L.F.G., 2014. The effect of deformation on the
32 690 TitaniQ geothermobarometer: An experimental study. *Contributions to Mineralogy and*
33 691 *Petrology* 167, 1–22. <https://doi.org/10.1007/s00410-014-0982-x>
34 692
- 35 692 Paterson, M.S., 2012. *Materials science for structural geology*. Springer Science & Business
36 693 *Media*.
37 694
- 38 694 Paterson, M.S., Luan, F.C., 1990. Quartzite rheology under geological conditions. *Geological*
39 695 *Society, London, Special Publications* 54, 299–307.
40 696
- 41 696 Pearce, M.A., Wheeler, J., 2010. Modelling grain-recycling zoning during metamorphism.
42 697 *Journal of Metamorphic Geology* 28, 423–437. [https://doi.org/10.1111/j.1525-](https://doi.org/10.1111/j.1525-1314.2010.00872.x)
43 698 [1314.2010.00872.x](https://doi.org/10.1111/j.1525-1314.2010.00872.x)
44 699
- 45 699 Perny, B., Eberhardt, P., Ramseyer, K., Mullis, J., Pankrath, R., 1992. Microdistribution of Al,
46 700 Li, and Na in α quartz: Possible causes and correlation with short-lived
47 701 cathodoluminescence. *American Mineralogist* 77, 534–544.
48 702
- 49 702 Piazzolo, S., Prior, D.J., Holness, M.D., 2005. The use of combined cathodoluminescence and
50 703 EBSD analysis: a case study investigating grain boundary migration mechanisms in quartz.
51 704 *J Microsc* 217, 152–161.
52 705
- 53 705 Poirier, J.-P., Guillopé, M., 1979. Deformation induced recrystallization of minerals. *Bulletin de*
54 706 *Mineralogie* 102, 67–74.
55 707
56
57
58
59
60
61
62
63
64
65

- 707 Poirier, J. P. (1985), *Creep of Crystals: High-Temperature Deformation Processes in Metals,*
1 708 *Ceramics and Minerals*, 260 pp., Cambridge Univ. Press, Cambridge, U. K.
- 2
3 709 Pongrac, P., Jeřábek, P., Stünitz, H., Raimbourg, H., Heilbronner, R., Racek, M., Nègre, L.,
4 710 2022. Mechanical properties and recrystallization of quartz in presence of H₂O:
5 711 Combination of cracking, subgrain rotation and dissolution-precipitation processes. *J Struct*
6 712 *Geol* 160. <https://doi.org/10.1016/j.jsg.2022.104630>
- 8
9 713 Précigout, J., Stünitz, H., Pinquier, Y., Champallier, R., Schubnel, A., 2018. High-pressure,
10 714 high-temperature deformation experiment using the new generation griggs-type apparatus.
11 715 *Journal of Visualized Experiments* 2018. <https://doi.org/10.3791/56841>
- 12
13 716 Qi, C., Goldsby, D.L., Prior, D.J., 2017. The down-stress transition from cluster to cone fabrics
14 717 in experimentally deformed ice. *Earth Planet Sci Lett* 471, 136–147.
15 718 <https://doi.org/10.1016/j.epsl.2017.05.008>
- 16
17 719 Raimbourg, H., Rajič, K., Moris-Muttoni, B., Famin, V., Palazzin, G., Fisher, D., Morell, K.,
18 720 Erdmann, S., Di Carlo, I., Montmartin, C., 2021. Quartz Vein Geochemistry Records
19 721 Deformation Processes in Convergent Zones. *Geochemistry, Geophysics, Geosystems* 22.
20 722 <https://doi.org/10.1029/2020GC009201>
- 22
23 723 Raj, R., Ashby, M.F., 1971. On grain boundary sliding and diffusional creep. *Metallurgical*
24 724 *transactions* 2, 1113–1127.
- 25
26 725 Richter, B., Stünitz, H., Heilbronner, R., 2018. The brittle-to-viscous transition in polycrystalline
27 726 quartz: An experimental study. *J Struct Geol* 114, 1–21.
28 727 <https://doi.org/10.1016/j.jsg.2018.06.005>
- 29
30 728 Rutter, E.H., Brodie, K.H., 2004a. Experimental grain size-sensitive flow of hot-pressed
31 729 Brazilian quartz aggregates. *J Struct Geol* 26, 2011–2023.
32 730 <https://doi.org/10.1016/j.jsg.2004.04.006>
- 33
34 731 Rutter, E.H., Brodie, K.H., 2004b. Experimental intracrystalline plastic flow in hot-pressed
35 732 synthetic quartzite prepared from Brazilian quartz crystals. *J Struct Geol* 26, 259–270.
36 733 [https://doi.org/10.1016/S0191-8141\(03\)00096-8](https://doi.org/10.1016/S0191-8141(03)00096-8)
- 37
38
39 734 Rutter, E.H., Brodie, K.H., 1988. The role of tectonic grain size reduction in the rheological
40 735 stratification of the lithosphere. *Geologische Rundschau* 77, 295–307.
41 736 <https://doi.org/10.1007/BF01848691>
- 42
43 737 Rybacki, E., Paterson, M.S., Wirth, R., Dresen, G., 2003. Rheology of calcite–quartz aggregates
44 738 deformed to large strain in torsion. *J Geophys Res Solid Earth* 108.
45 739 <https://doi.org/10.1029/2002jb001833>
- 46
47 740 Samae, V., Cordier, P., Demouchy, S., Bollinger, C., Gasc, J., Koizumi, S., Mussi, A.,
48 741 Schryvers, D., Idrissi, H., 2021. Stress-induced amorphization triggers deformation in the
49 742 lithospheric mantle. *Nature* 591, 82–86. <https://doi.org/10.1038/s41586-021-03238-3>
- 50
51 743 Schmid, S.M., 1982. Laboratory experiments on rheology and deformation mechanisms in
52 744 calcite and their application to studies in the field. *Mitteilungen des Geologischen Institutes*
53 745 *der ETH Universität. Zürich*, 241, p.1.
- 54
55
56 746 Stipp, M., Fügenschuh, B., Gromet, L.P., Stünitz, H., Schmid, S.M., 2004. Contemporaneous
57 747 plutonism and strike-slip faulting: A case study from the Tonale fault zone north of the
58 748 Adamello pluton (Italian Alps). *Tectonics* 23. <https://doi.org/10.1029/2003TC001515>
- 59
60
61
62
63
64
65

- 749 Stipp, M., Tullis, J., 2003. The recrystallized grain size piezometer for quartz. *Geophys Res Lett*
 1 750 30. <https://doi.org/10.1029/2003GL018444>
 2
- 3 751 Stipp, M., Tullis, J., Behrens, H., 2006. Effect of water on the dislocation creep microstructure
 4 752 and flow stress of quartz and implications for the recrystallized grain size piezometer. *J*
 5 753 *Geophys Res Solid Earth* 111. <https://doi.org/10.1029/2005JB003852>
 6
- 7 754 Stünitz, H., Thust, A., Heilbronner, R., Behrens, H., Kilian, R., Tarantola, A., Fitz Gerald, J.D.,
 8 755 2017. Water redistribution in experimentally deformed natural milky quartz single
 9 756 crystals—Implications for H₂O-weakening processes. *J Geophys Res Solid Earth* 122,
 10 757 866–894. <https://doi.org/10.1002/2016JB013533>
 12
- 13 758 Tailby, N.D., Cherniak, D.J., Watson, E.B., 2018. Al diffusion in quartz. *American Mineralogist*
 14 759 103, 839–847. <https://doi.org/10.2138/am-2018-5613>
 15
- 16 760 Tokle, L., Hirth, G., Behr, W.M., 2019. Flow laws and fabric transitions in wet quartzite. *Earth*
 17 761 *Planet Sci Lett* 505, 152–161. <https://doi.org/10.1016/j.epsl.2018.10.017>
 18
- 19 762 Tullis, J. and Yund, R.A., 1989. Hydrolytic weakening of quartz aggregates: The effects of
 20 763 water and pressure on recovery. *Geophysical Research Letters*, 16(11), pp.1343-1346.
 21
- 22 764 Tullis, J. and Yund, R.A., 1982. Grain growth kinetics of quartz and calcite aggregates. *The*
 23 765 *Journal of Geology*, 90(3), pp.301-318.
 24
- 25 766 Urai, J.L., Means, W.D., Lister, G.S., 1986. Dynamic recrystallization of minerals. *Mineral and*
 26 767 *rock deformation: laboratory studies* 36, 161–199.
 27
- 28 768 White, S.H., Burrows, S.E., Carreras, J., Shaw, N.D., Humphreys, F.J., 1980. On mylonites in
 29 769 ductile shear zones. *J Struct Geol* 2, 175–187. [https://doi.org/https://doi.org/10.1016/0191-](https://doi.org/https://doi.org/10.1016/0191-8141(80)90048-6)
 30 770 8141(80)90048-6
 31
- 32 771 Wilkinson, D.S., Cáceres, C.H., 1984. On the mechanism of strain-enhanced grain growth
 33 772 during superplastic deformation. *Acta Metallurgica* 32, 1335–1345.
 34 773 [https://doi.org/https://doi.org/10.1016/0001-6160\(84\)90079-8](https://doi.org/https://doi.org/10.1016/0001-6160(84)90079-8)
 35 774
 36
- 37 774 Yabe, K., Sueyoshi, K., Hiraga, T., 2020. Grain-Boundary Diffusion Creep of Olivine: 1.
 38 775 Experiments at 1 atm. *J Geophys Res Solid Earth* 125.
 39 776 <https://doi.org/10.1029/2020JB019415>
 40
- 41 777 Yuan, M.-W., Li, L., Alam, M., Santosh, M., Li, S.-R., Hou, Z.-Q., 2023. Correlations between
 42 778 cathodoluminescence intensity and aluminum concentration in low-temperature
 43 779 hydrothermal quartz. *American Mineralogist* 108, 1224–1231. [https://doi.org/10.2138/am-](https://doi.org/10.2138/am-2022-8471)
 44 780 2022-8471
 45 780
 46
 47 781
 48

782 **Figure captions**

50
 51 783 **Figure 1. Microstructural characterization of undeformed novaculite performed on a**
 52 784 **cylindrical core oriented parallel to the intended compression direction. a** Cross-polarized light-
 53 785 microphotograph showing sporadically distributed large quartz clasts (yellow arrow) and micas (pink
 54 786 arrow). **b** BSE image that reveals a typical homogeneous microstructure. **c** Cathodoluminescence
 55 787 (CL) image that indicates a largely homogeneous initial colour spectrum of quartz grains. The
 56 788 corresponding spectra with a very prominent peak at 650 nm are shown in Supplementary Fig. 5. **d**
 57 789 CL spectra with a very prominent peak at ~650 nm corresponding to different luminescence (yellow
 58 790 to slightly blueish) seen in the previous CL map. A very subdue peak can be observed between 375
 59
 60
 61
 62
 63
 64
 65

and 400 nm. **e** EBSD misorientation map showing grains mostly free of internal strain. Three types of boundaries are plotted: i) high-angle grain boundaries (black lines) defined by misorientation angle, ii) low-angle boundaries defined by misorientations between 2 to 10°, including continuous sub-grain boundaries (green lines), and discontinuous inner boundaries (pink lines). Sub-grain boundaries form closed polygons, while inner boundaries do not. **f** Pole figure of the *c*-axis orientation highlighting no preferred orientation. **g** Quantified shape fabric in terms of particle ODF (PAROR) (ODF with maximum indicated on the figure, 10 contours 0.5 - 5.0) on a rose diagram (supplementary text). The bulk *b/a* is indicative of the shape anisotropy of the quartz grains. *b/a* = 1 indicates that the bulk shape of the particles is close to a circle while the lower values until '0' indicate a progressive increase in anisotropy. **h** Histograms of 2D and 3D grain size distribution of quartz grains.

Figure 2. Experimental setup and Mechanical data. **a** Schematic diagram of the coaxial experimental set-up in the new generation Griggs apparatus. **b** A typical stress-strain-time data (OR107) obtained during load-stepping experiment at 900 °C and 1 GPa. **c** A typical stress-strain-time data obtained during temperature-steeping (900 to 750 °C) at constant load and 1 GPa confining pressure (OR111). **d** Stress-strain curves for constant strain rate experiments. σ and $\dot{\epsilon}$ values are calculated from the peak strength portion of the mechanical curve. **e** Determination of stress exponent (*n*) in a log-log space from load-stepping experiments (as-is, H₂O-added, and dry). The slope of the global fit indicates the *n*-value. **f** Arrhenius plot for the determination of the activation energy (*Q*) using the as-is constant-load experiment.

Figure 3. Microstructural and chemical observations from the central portion of the as-is (691) and 0.1% H₂O-added (689) samples deformed under constant $\dot{\epsilon}$. The long axis orientation (i.e., compression direction) of the cylindrical novaculite cores is vertical (white arrow). **a-b** The locations of the EBSD maps are marked as white box on the CL figures. Intragranular misorientations ("mis2mean" function in MTEX) of quartz grains are shown. Slightly finer grains corresponding to the CL-yellow areas correspond to non-indexing problem in the EBSD maps. The corresponding Al map shows a positive correlation with the CL colours. Also, see Supplementary Fig. 6 corresponding to a different location from H₂O-added sample. **c** The 3D grain size distribution (GSD) remains 'broadly' unimodal. Pole figures of the *c*-axis orientation show random fabric (ODF with maximum indicated on the figures, 10 contours 0.5 - 5.0). The PAROR rose diagram shows the development of a strong SPO in the deformed samples.

Figure 4. Microstructural and chemical observations from the central portion of the samples deformed under constant load. **a-c** Deformed H₂O-added sample that shows a homogeneously dispersed core-shell microstructure (b) and grain size distribution (a). A third darker luminescence (b) is better observed between the bright blue and yellow color in CL within individual grains. Notice that the CL-yellow or the Al-poor (c) cores are of different sizes and not always located at the centre of the individual grains. BSE image shows that the porosity (yellow arrow) is pervasively developed through the sample. **d-f** Deformed as-is sample shows patchily developed CL-blue (e) that generally correspond to the larger grains (d) with higher Al content (f). Inside of a few grains, the original CL-yellow luminance was preserved which forms the core-shell microstructure of individual grains. Porosity is not developed in the zones containing finer grains (~ CL-yellow) with low Al content. **g-i** Deformed dry sample that shows a significant portion of the image where the finer grains correspond with CL-yellow luminescence (h). In comparison to the as-is sample, the CL-yellow zones witnessed some porosity development. The bright phases (with high Ti content) marked by the red arrow and the open grain boundaries marked by the green arrow in BSE (g) are exaggerated by the red color in WDS (i). Larger holes represent plucked grains from sample preparation. Further information about microstructural and chemical features of the deformed samples are also available in supplementary Figs. 4 and 5.

Figure 5. Typical CL spectra of core-shell structures in the H₂O-added sample. While the reconstituted brighter blue shell shows a similar spectra pattern (with new prominent peaks between

840 350 and 475 nm) as the darker blue shell, the yellow core shows a very prominent peak at 650 nm,
841 similar to the undeformed novaculite as shown in Figure 1d.

842 **Figure 6. Microstructural and chemical observations from the central portion of the**
843 **deformed and undeformed novaculite samples. a** Al content across several quartz grains with
844 different CL luminescence using EPMA point analyses. The inset CL image is taken from
845 the H₂O-added deformed sample shown in supplementary Figure 4b. **b** Map distribution of Ca,
846 Na, and K in a representative area of the H₂O-rich deformed sample. Grain boundaries are
847 highlighted by element concentrations along them. **c** Na⁺ and K⁺ *versus* Al³⁺ in quartz grains
848 across an EPMA line transect located on the CL map of the H₂O-added deformed sample. **d** Al
849 *versus* H (normalized to 10⁶Si) of quartz grains in all samples using SIMS point analyses. This
850 graph indicates a positive correlation between H/10⁶Si and Al/10⁶Si. Notice the original
851 undeformed novaculite is dried at 110° C for one day. **e and f** BSE images of representative areas in
852 the H₂O-added sample. They highlight a porosity development along grain boundaries and
853 junctions (yellow arrows), as well as curved grain boundaries (green arrows) that are
854 indicative of grain boundary migration (GBM). **g** EBSD band contrast map of a representative
855 area in the as-is sample. The map documents grain boundaries (red lines plotted using MTEX)
856 with unequivocal presence of four-grain junctions (white arrows), commonly indicative of grain
857 boundary sliding

857 **Figure 7. Microstructural and chemical observations of the as-is and deformed samples. a**
858 Forescattered electron (FSE) image from the top portion of the as-is (constant- $\dot{\epsilon}$) sample. A very
859 restricted porosity development is observed. **b** Corresponding CL map that shows a very limited
860 reconstitution of grain boundaries in comparison to the microstructural observations described in
861 Figures 4 to 6. **c** Corresponding EBSD map of intragranular misorientations, which give rise to
862 limited internal crystal-plastic deformation, although PAROR analysis indicates the development of a
863 weak SPO. **d** BSE and CL images, as well as distribution of Al and Fe in a representative area of the
864 super-dry deformed sample. In contrast to the other experiments (as-is, H₂O-added, and dry), the
865 super-dry sample retains most of the original CL-yellow luminescence. We also observed fluid
866 (melt?) pockets and mica-rich zones in contrast to other deformed samples.

867 **Figure 8. Comparison of the mechanical data (σ and $\dot{\epsilon}$) with previous studies.** The red lines and
868 the transparent data points are calculated using the coarse-grained, 0.1 wt. % H₂O-added Tana flow
869 law (equation 2) (Ghosh et al., 2022). **a** Log-log graph of stress *versus* strain rate of the as-is
870 novaculite samples. The as-is novaculite is ~ 4.5 times weaker than the as-is Tana quartzite, but shows
871 a similar stress exponent ($n \approx 2$). Notice that if we do not consider the lowest stress point for the as-is
872 novaculite experiment, then the n -value becomes ~1.99 from a value of 2.19 (Fig. 2d). **b** Log-log
873 graph of stress *versus* strain rate of the H₂O-added novaculite sample. The latter is here documented as
874 ~ 4 times weaker than Tana quartzite based on the flow law from Ghosh et al., (2022). **c** Log-log
875 graph of stress *versus* strain rate of the dry novaculite sample. In this case, the novaculite is slightly (~
876 1.4 times) stronger than Tana quartzite considering equation 2. **d** In the Arrhenius $\ln(\dot{\epsilon}) - T^{-1}$ space,
877 the data from as-is novaculite is similar to the values calculated from the Tana flow law. **e** Non-
878 dimensional plot of strain rate ($\dot{\epsilon}_0$) *versus* stress (σ_0) compiling the original mechanical data (σ and $\dot{\epsilon}$)
879 reported in the literature: Kronenberg and Tullis (1984; K&T84); Heilbronner and Kilian (2017; H&K
880 02); Rutter and Brodie (2004a and b; R&B04a,b); Stipp et al. (2006; Stipp 06); Kidder et al. (2016;
881 Kidder 16); Fukuda et al. (2018; Fukuda 18); Richter et al. (2018; Richter 18). Only the results that
882 satisfy the Goetze criterion have been included. Most of the creep results obtained from previous
883 coarse- or fine-grained quartz aggregates overlaps with or follow our novaculite and Tana quartzite
884 datasets, even the absolute strengths are essentially comparable (within a factor of ~5 times the $\dot{\epsilon}$,
885 indicated by the shaded region drawn from Fig. 7a of Ghosh et al., 2022).

887 **Figure 9. Model of grain boundary processes occurring during plastic deformation of quartz**
888 **aggregates.** The undeformed grain boundaries were non-planar and the neighboring grains might
889 have different dislocation densities (i). Dissolution-precipitation through grain boundary H₂O between
890 adjacent grains and concurrent exchange of elements resulted in grain boundary migration (GBM) and

891 the observed CL luminescence (ii). In a transient state, four-grain junctions and porosity can develop
 892 during grain boundary sliding (GBS). While the red colour indicates where porosity develops,
 893 the violet colour indicates the filling up of porosity with progressive deformation and precipitation.

894

895

896

897

898

899 Table 1. Summary of the Experimental results.

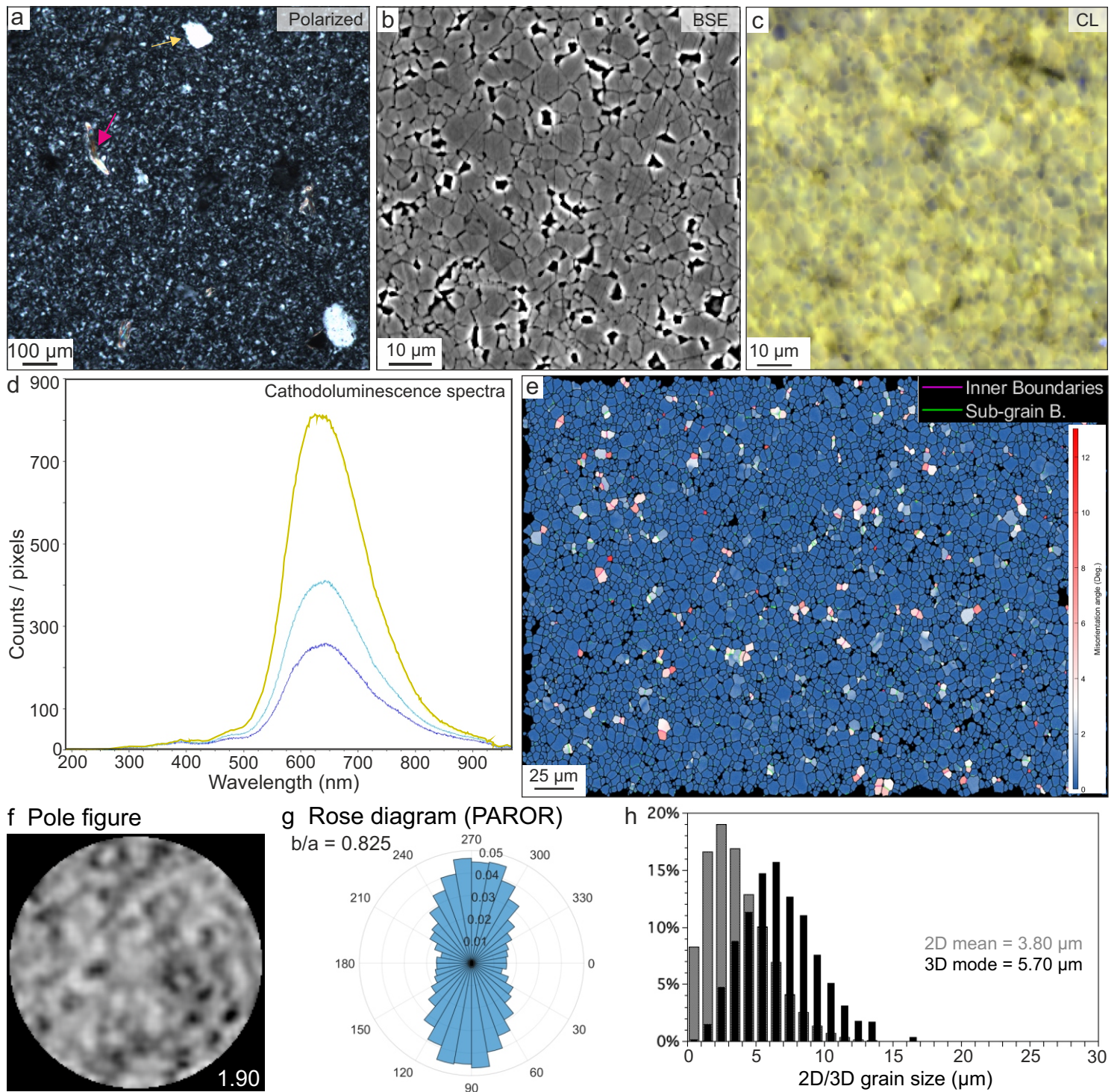
Experiment	T	H ₂ O	Height	σ	$\dot{\epsilon}$	Duration	Final ϵ	$d_{2D(mean)}$	$d_{3D(mean)}$
	(°C)	(wt. %)	(mm)	(MPa)	(s ⁻¹)	(hr)	(%)	μm^*	μm
OR105	900	0.1	15.03	105.08	1.63E-06	~27.88	11.67	6.40	10.20
				157.54	2.95E-06				
				198.75	4.19E-06				
				20.56	6.11E-08				
				66.82	4.24E-07				
OR107	900	as-is	15.01	136.55	9.94E-07	~148.55	18.26	6.50	12.6
				76.82	2.86E-07				
				42.59	7.49E-08				
				183.67	1.33E-06				
				224.40	1.89E-06				
				263.37	2.57E-06				
				75.31	1.40E-07				
				130.61	4.78E-07				
				182.39	1.13E-06				
				222.16	1.76E-06				
42.33	2.91E-08								
OR113	900	dry	15.02	62.17	1.43E-07	~149.61	21.30	6.20	11.8
				159.43	7.72E-07				
				205.44	1.15E-06				
				100.10	2.25E-07				
				251.96	1.67E-06				
				127.28	2.82E-07				
				244.21	1.53E-06				
				283.00	2.19E-06				
				171.51	8.39E-07				
				282.73	2.10E-06				
OR116	900	super-dry	14.77	-	-	~196.20	-	4.06 ^s	6.22 ^s
OR111	900	as-is	14.98	158.79	8.04E-07	~198.47	18.52	-	-
	850			154.86	5.09E-07				
	800			150.35	2.83E-07				
	750			146.86	1.36E-07				
689	900	0.1	12.71	185.48 [#]	1.18E-06	~39.86	16.50	3.74	6.18
691	900	as-is	12.73	174.17 [#]	1.31E-06	~43.66	20.30	3.72	6.41

1 900 *Initial grain size is 3.80 μm in 2D and 5.70 μm in 3D. The 2D mean grain sizes are shown to have parity with the previous
2 901 studies. The 3D mode can be found in the histograms.

3 902 #Peak stress values are shown.

4 903 §For the 'superdry' sample the initial undeformed grain size after annealing and the final deformed grain size
5 904 does not show any variation.

6
7
8
9
10
11
12
13
14
15
16
17
18
19
20
21
22
23
24
25
26
27
28
29
30
31
32
33
34
35
36
37
38
39
40
41
42
43
44
45
46
47
48
49
50
51
52
53
54
55
56
57
58
59
60
61
62
63
64
65



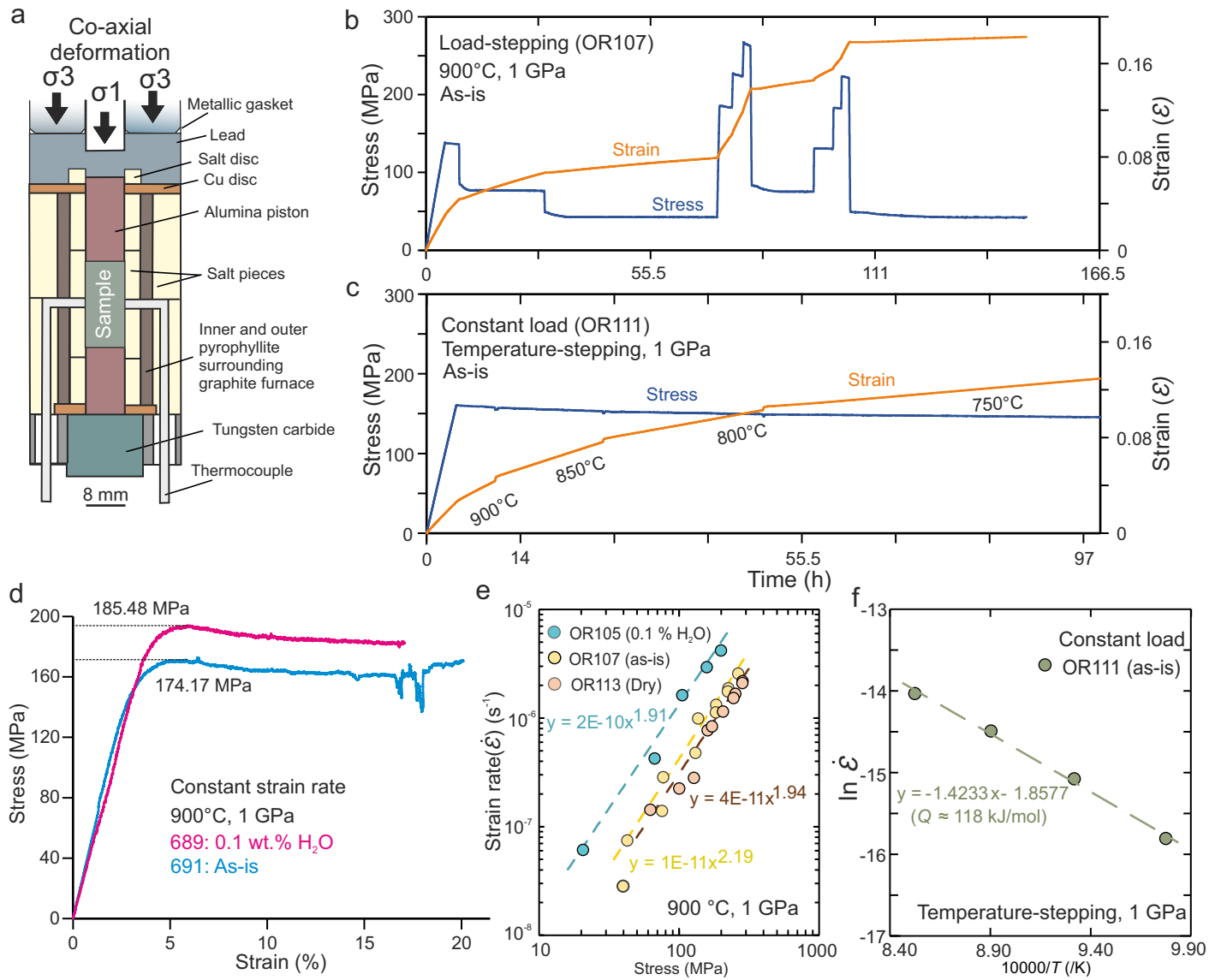
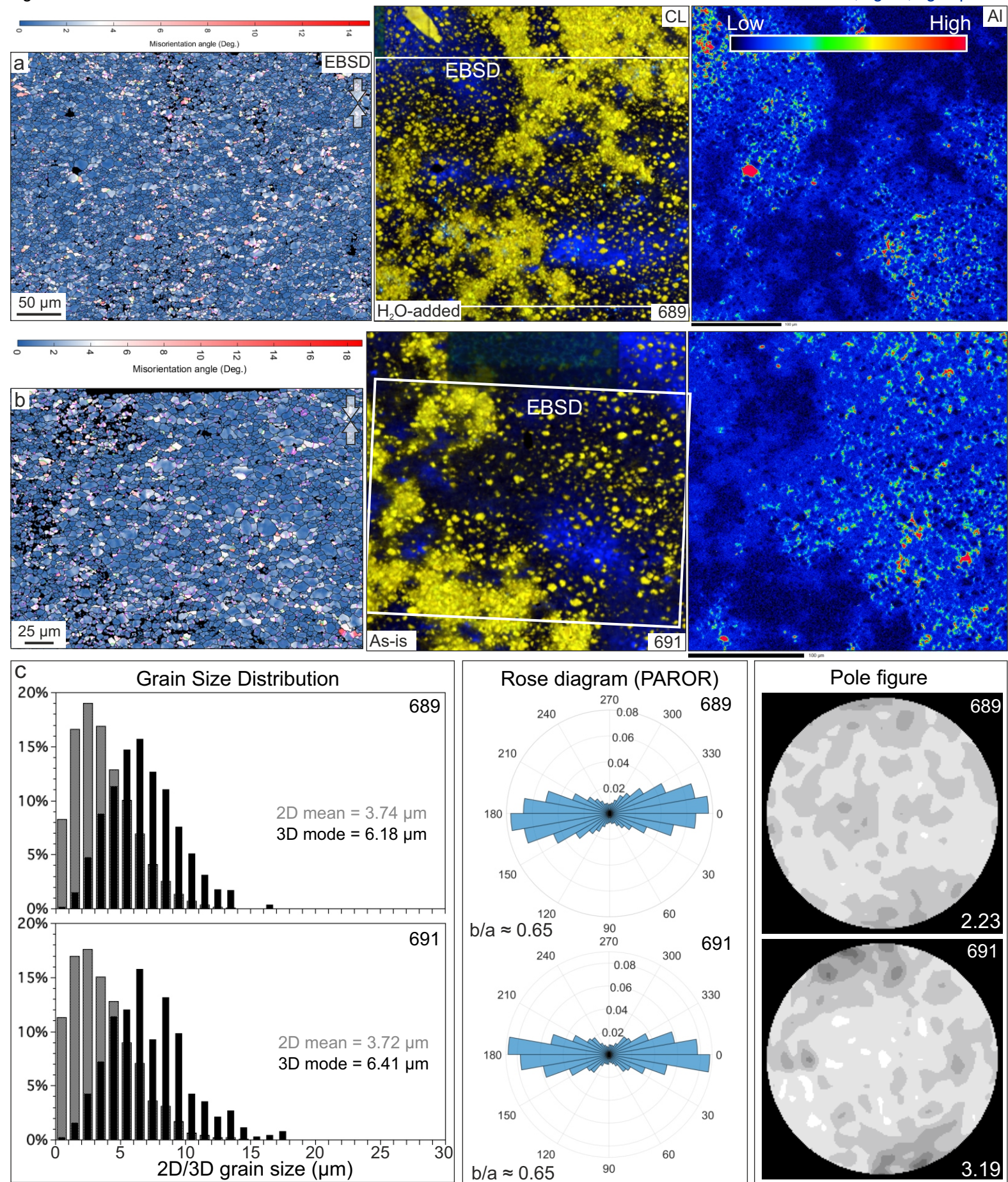
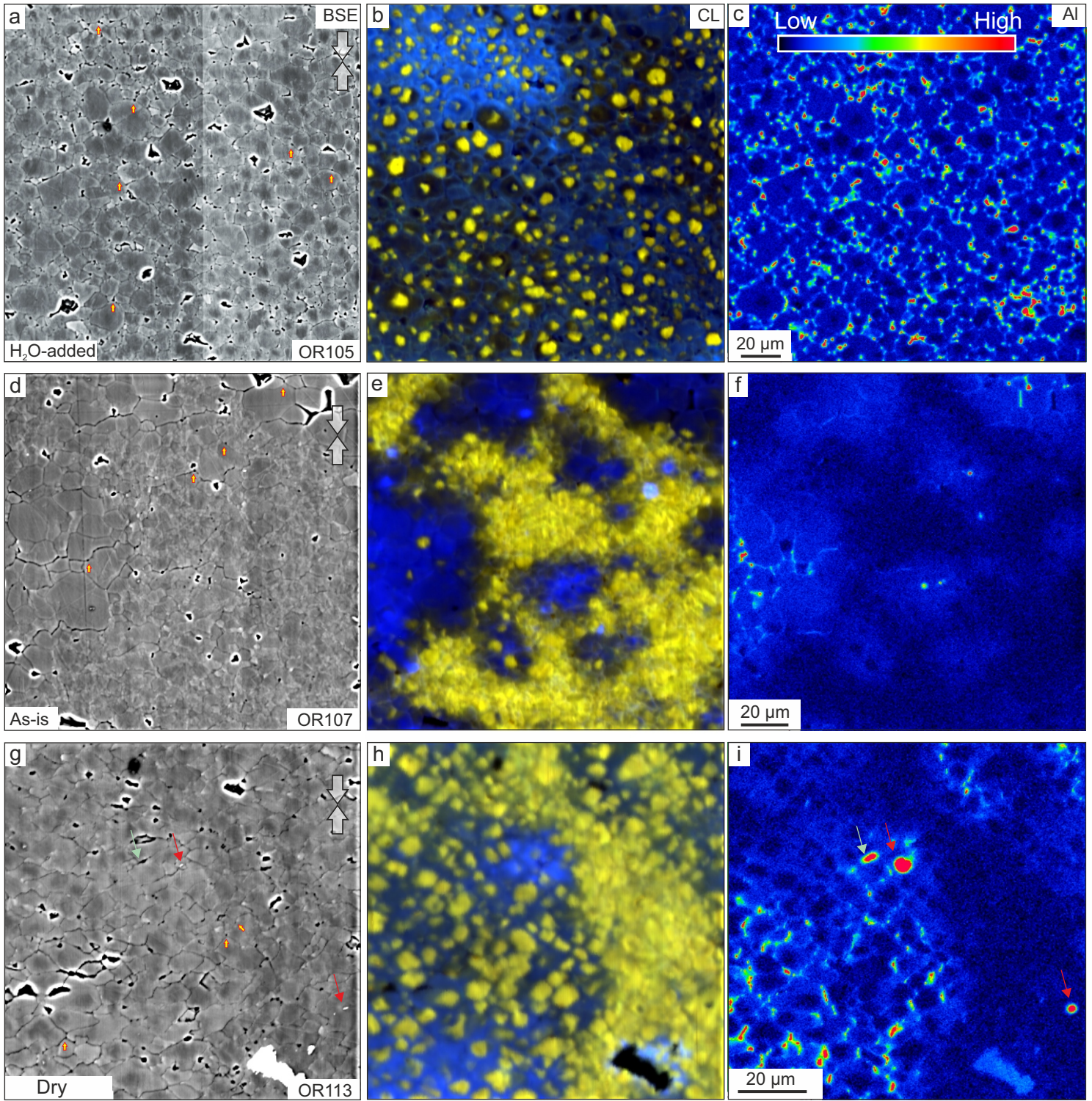
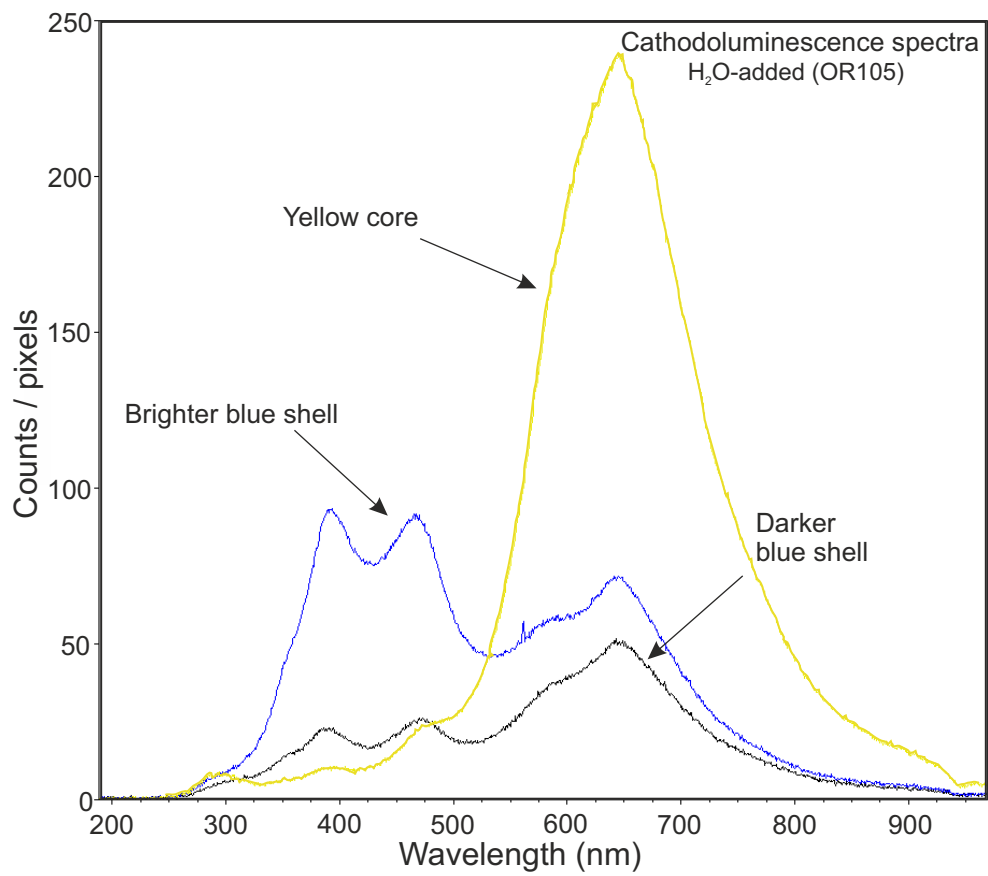


Figure 3







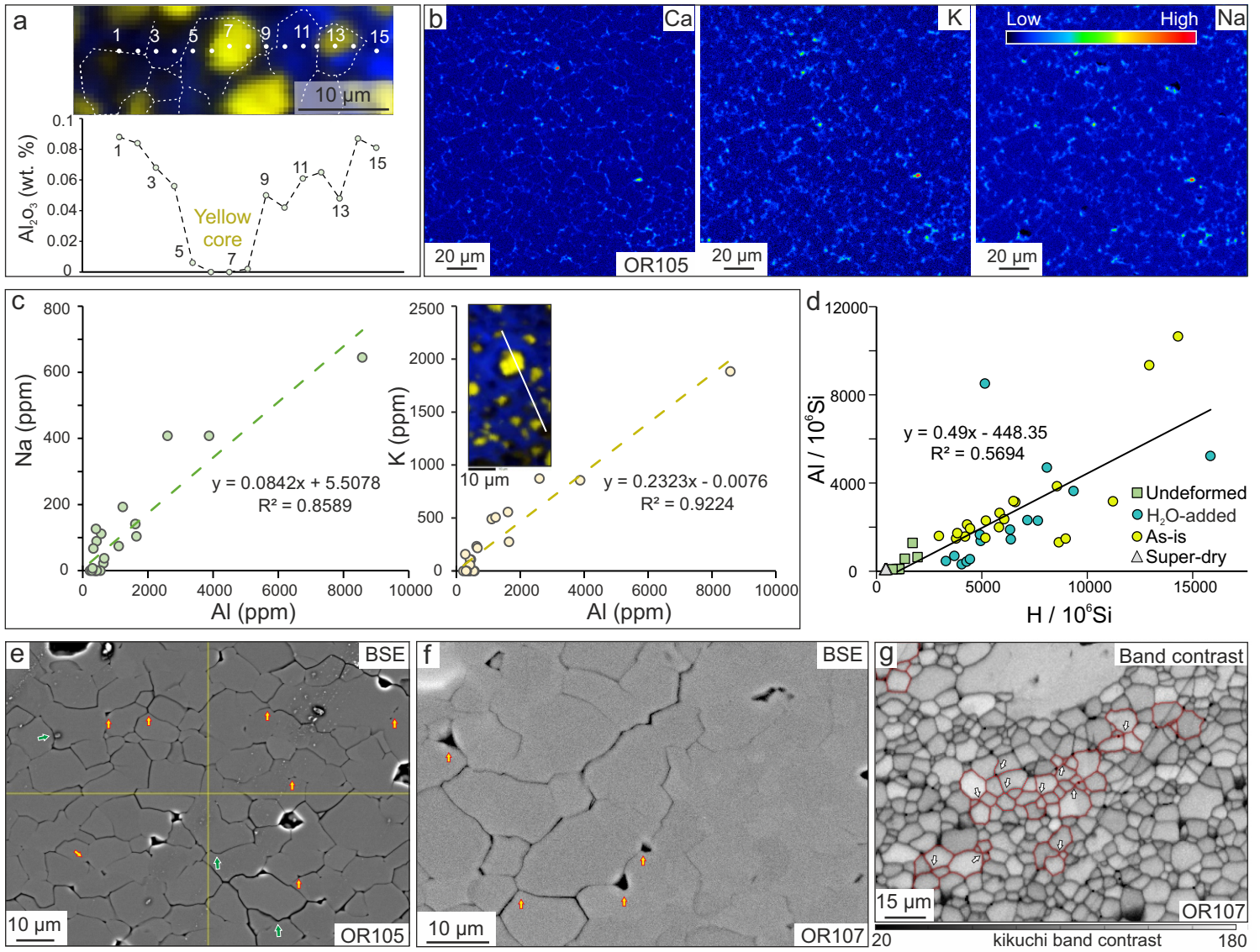
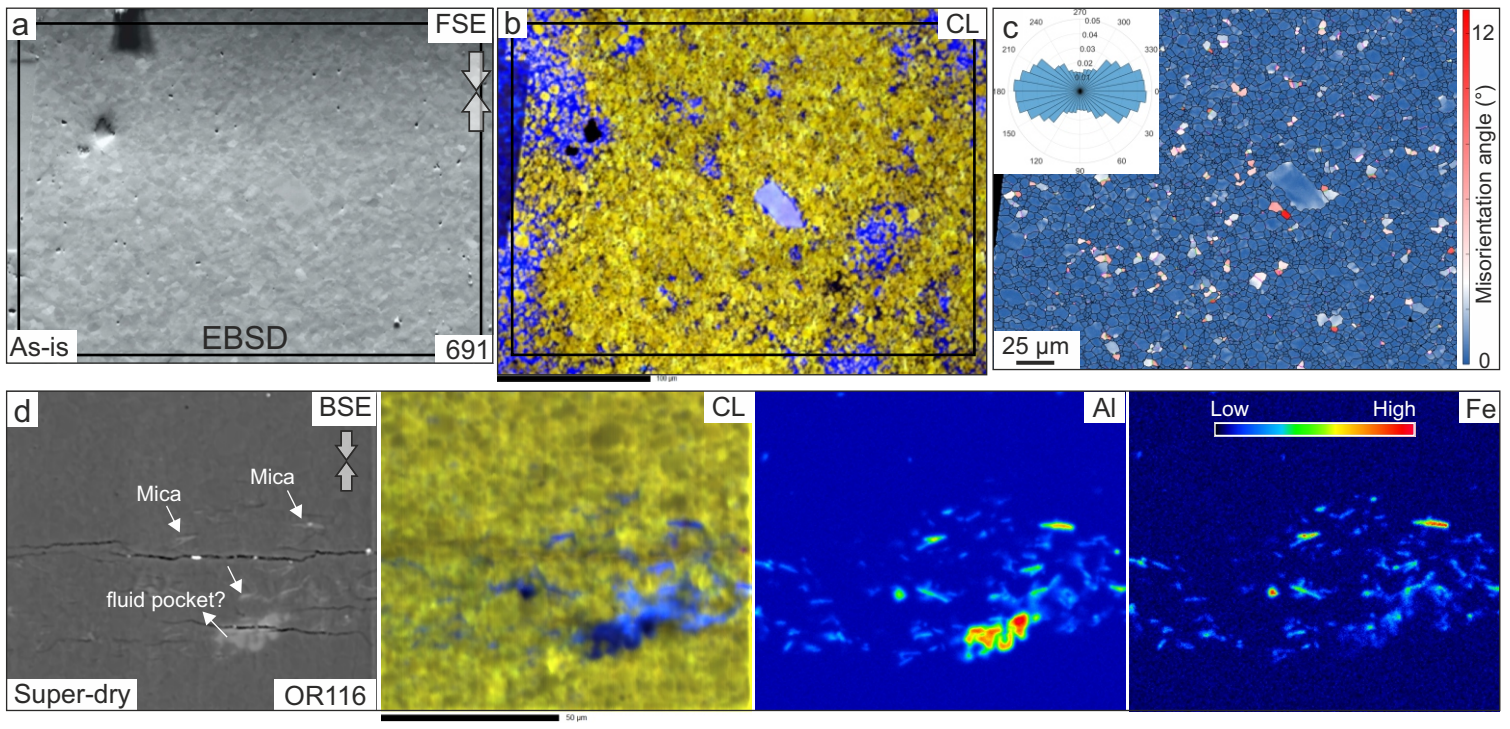
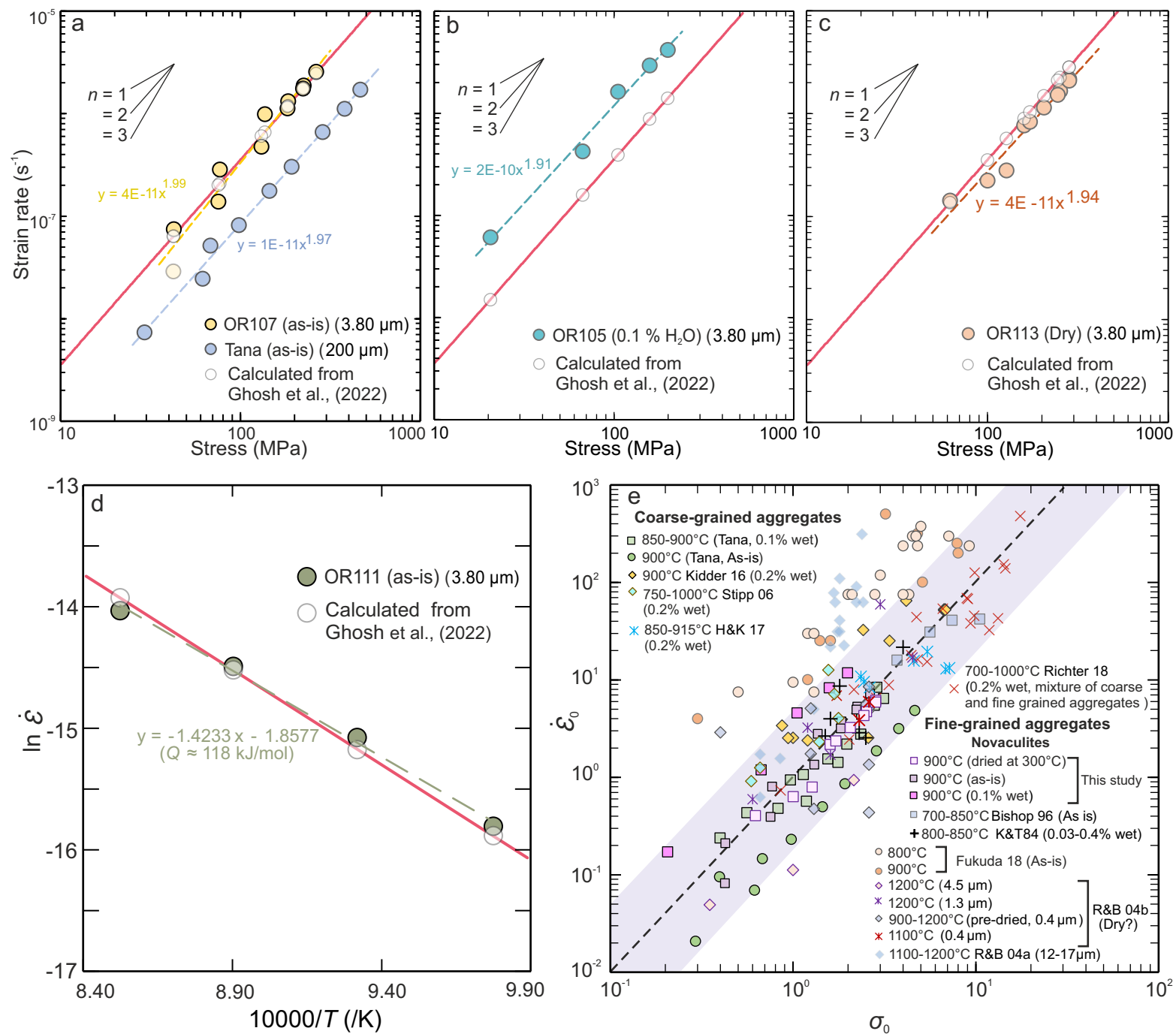
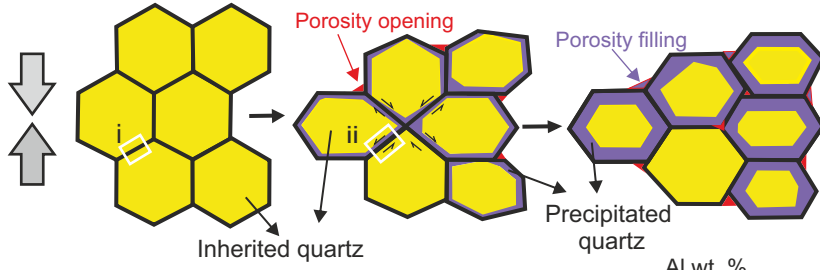


Figure 7

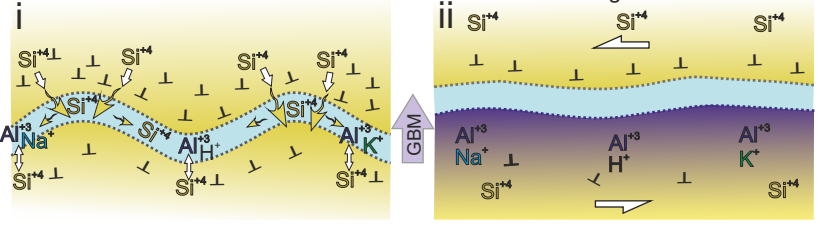




Serial grain boundary processes = Dissolution-precipitation
+ GBM + GBS + porosity development



↔ Substitution of Si^{4+} by Al^{3+} and $Na^+ / K^+ / H^+$



Declaration of interests

The authors declare that they have no known competing financial interests or personal relationships that could have appeared to influence the work reported in this paper.

The authors declare the following financial interests/personal relationships which may be considered as potential competing interests: